ORIGINAL PAPER

A Thermal–Hydraulic–Mechanical–Chemical Coupling Model for Acid Fracture Propagation Based on a Phase-Field Method

Yifan Dai[1,2,5] · Bing Hou[1,3] · Sanghyun Lee[4] · Thomas Wick[5]

Abstract

Acid fracturing is a technique to enhance productivity in carbonate formations. In this work, a thermal–hydraulic–mechanical–chemical (THMC) coupling model for acid fracture propagation is proposed based on a phase-field approach. The phase-field variable is utilized as an indicator function to distinguish the fracture and the reservoir, and to track the propagation of the fracture. The resulting system is a nonstationary, nonlinear, variational inequality system in which five different physical modules for the displacement, the phase-field, the pressure, the temperature, and the acid concentration are coupled. This multi-physical system includes numerical challenges in terms of nonlinearities, solution coupling algorithms, and computational cost. To this end, high fidelity physics-based discretizations, parallel solvers, and mesh adaptivity techniques are required. The model solves the phase-field and the displacement variables by a quasi-monolithic scheme and the other variables by a partitioned schemes, where the resulting overall algorithm is of iterative coupling type. In order to maintain the computational cost low, the adaptive mesh refinement technique in terms of a predictor-corrector method is employed. The error indicators are obtained from both the phase-field and concentration approximations. The proposed model and the computational robustness were investigated by studying fourteen cases as well as some mesh refinement studies. It is observed that the acid and thermal effect increase the fracture volume and fracture width. Moreover, the natural fractures and holes affect the acid fracture propagation direction.

Highlights

- thermal–hydraulic–mechanical–chemical coupling system was established for acid fracture propagation based on a phase-field method.
- The acid fluid equations including diffusion, transport and reaction were derived. The penalization method was introduced based on physical reality.
- Acid fracture problem is a kind of dynamic heterogeneous problem. The adaptive mesh refinement was extended to help researchers get smooth simulation results and save computation costs.

✉ Bing Hou
  binghou@vip.163.com

  Yifan Dai
  819673313@qq.com

  Sanghyun Lee
  slee17@fsu.edu

  Thomas Wick
  thomas.wick@ifam.uni-hannover.de

1 National Key Laboratory of Petroleum Resources and Engineering, China University of Petroleum(Beijing), Fuxue road 18 Changping, Beijing, China

2 Ministry of Education Key Laboratory of Petroleum Engineering, China University of Petroleum(Beijing), Fuxue road 18 Changping, Beijing, China

3 Department of Petroleum Engineering, China University of Petroleum(Beijing) at Karamay, Karamay 834000, Xinjiang, China

4 Department of Mathematics, Florida State University, 1017 Academic Way, Tallahassee, FL 32306-4510, USA

5 Institut für Angewandte, Mathematik, AG Wissenschaftliches Rechnen, Leibniz Universität Hannover, Welfengarten 1, 30167 Hannover, Germany

List of Symbols

Symbols and Meanings

Λ	Smooth open and bounded computational domain
$\partial\Lambda$	Boundary of computational domain
t	Computational time interval
T	Final computational time
f	Lower dimensional fracture
Ω_F, Ω_R	Fracture and reservoir sub-domains in Λ
ε	Half thickness of the fracture edge area
∂F	Fracture interface in Λ
ϕ	Phase-field variable
$\mathbf{u}$	Vector-valued displacement
p	Scalar-valued pressure
Θ	Scalar-valued temperature
c	Scalar-valued acid concentration
ρ_F, ρ_R	Fracture and reservoir densities
ρ_{Ff}	Fluid densities in fracture
ρ_{Rf}, ρ_{Rr}	The rock and fluid densities in reservoir
φ_F^*, φ_R^*	Porosity of fracture and reservoir
$\text{Cap}_F, \text{Cap}_R$	Heat capacities of fracture and reservoir
K_{Fd}, K_{Rd}	Thermal diffusion coefficient of reservoir and fracture
V_F, V_R	Fluid velocities in the fracture and reservoir
$q_{F\Theta}, q_{R\Theta}$	Source terms of temperature equation
q_L	Leak-off terms of pressure equation
M	Biot's modulus
α	Biot's coefficient
K_{tc}	Thermal expansion coefficient of pores
K_{etch}	Acid etching coefficient
R_c	Acid–rock reaction term
t_{etch}	Etching time at any fixed points
η_F, η_R	Fluid viscosities in fracture and reservoir
K_F, K_R	Permeabilities in fracture and reservoir
K_{Ffc}, K_{Rfc}	Fluid compressibilities in fracture and reservoir
q_{Ff}, q_{Rf}	Fluid source terms
K_{Fc}, K_{Rc}	Acid diffusion coefficients
q_{Fc}, q_{Rc}	Acid source terms
K_{ar}	Acid–rock reaction rate speed
p_r	Reference pressure for acid reaction
Ea	Activation energy of reaction equation
R	Gas constant.
Θ_T	Absolute temperature (unit in Kelvin)
G_F	Critical energy release rate
$\sigma(\mathbf{u})$	Linear elastic stress tensor
σ_{eff}	Poroelastic stress tensor
$e(\mathbf{u})$	Strain tensor
λ, G	Lame coefficients
I	Second-order identity tensor
E	Young's modulus
ν	Poisson's ratio
$3\alpha_\Theta$	Thermal expansion coefficient.
k	Regularization parameter
C_Θ	Temperature relation constant near the fracture
σ^+	Tensile stress
σ^-	Compression stress
n	The outward normal vector of the domain Λ
f_p, f_Θ, f_c	Given boundary values
M_h	The mesh family, $h > 0$ is the mash size
χ_F, χ_R	The indicator functions for subdomain
D_f, D_r	The distinguishing indexes for fracture and reservoir
c_s	Saturation concentration of acid
γ_0, γ_s	Penalization terms
TH_ϕ, TH_c	Thresholds for adaptive mesh refinement
$Res(\cdot)$	Residual of each PDE system
TOL_s, TOL_{fs}	The solver tolerance

Abbreviations and Meanings

THMC	Thermal–hydraulic–mechanical–chemical
QOI	Quantities of interest
FV	Fracture volume
COD	Crack opening displacements
AC	Acid consumption

1 Introduction

Acid fracturing is a technique to enhance the oil and natural gas production in carbonate reservoirs (Liu et al. 2014; Hou et al. 2019). The acid fluid would be injected into the wellbore as the fracturing fluid, which would increase the pressure in the wellbore and form artificial fractures. During this process, the acid would react with the rock around the fractures, reducing the rock strength and making it easy for propagation (Guo et al. 2014; Hou et al. 2021). Many researches have proven that acid fracturing in carbonate reservoirs is a multi-physics process. Several physical parameters, including fluid pressure, temperature, and acid concentration, would interact with each other (Khoei et al. 2012; Fan et al. 2019; Xu et al. 2021).

There are many studies for thermal–hydraulic–mechanical–chemical (THMC) coupling problems, including gas hydrate-bearing sediment (Gupta et al. 2017), methane hydrate formation and dissociation (Chong et al. 2016), and so on. Fei et al. (2023) studied the near-wellbore nucleation and propagation of hydraulic fractures in Enhanced geothermal systems. Poulet et al. (2012) studied the shear heating and damage

based on ESCRIPTRT and ABAQUS. The resulting THMC code was built on the two existing codes. Wu et al. (2023) built the THMC coupling model for carbon dioxide fracturing based on the COMSOL-MATLAB-PHREEQC (CMP) coupling framework. Ogata et al. (2018) built the THMC model to predict the permeability changes. The simulation result was compared with the flow-through experiments result. There are many related studies that deal with multiple physics phenomena and exceed classical hydraulic fracturing simulations (Min et al. 2023; Miehe et al. 2015c, a; Miehe and Mauthe 2016; Lee et al. 2016a, 2018a, 2017b). Different groups developed their own numerical models with different approaches. The interactions between multi-physical parameters are big challenges for the THMC coupling models, which often result in nonstationary, nonlinear systems (Wick 2020).

Multi-physics fracture propagation is one of the research focuses in the petroleum industry. Luo et al. (2020) studied acid fracture propagation in fractured-vuggy carbonate reservoirs based on the extended finite elements. This approach includes mechanical, hydro, and acid–rock reaction modules. Yu et al. (2019) took the heterogeneity and anisotropy of the reservoir into their model to study the fluid pressure-driven fracture. Khoei et al. (2012) used an enhanced function to describe the physical quantities on both sides of the fractures in a stress-seepage-temperature coupling fracture propagation model. There are different approaches for fracture propagation simulation, including level-set methods (Peirce and Detournay 2008), boundary element methods (Castonguay et al. 2013), partition-of-unity methods (Schrefler and Secchi 2012; Adachi et al. 2007; Gupta and Duarte 2014), variational/phase-field approaches (Francfort and Marigo 1998; Bourdin et al. 2000; Kuhn and Müller 2010; Miehe et al. 2010) and so on (Ghidelli et al. 2017; Gupta and Duarte 2016; Rabczuk et al. 2010; Takabi and Tai 2019; Lee et al. 2018b). These methods can be distinguished into the interface-tracking and interface-capturing methods (Wick 2020). In the interface-tracking method, the mesh would move with the fracture propagation and need to be updated every timestep, which brings difficulties in re-meshing and simulation. In the interface-capturing method, which phase-field methods belong to, the mesh is fixed and the fracture is described by additional functions, which solve the mesh degeneration problem and make it be implemented easily to simulate fracture nucleation, propagation, kinking, curvilinear path, branching, and joining. There are several summaries and overview monographs about the conclusions (Bourdin et al. 2008; Ambati et al. 2015; Wu et al. 2020; Bourdin and Francfort 2019; Diehl et al. 2022; Wick 2020).

There are many related research achievements for phase-field fractures in porous media (Chukwudozie et al. 2019; Miehe and Mauthe 2016; Wilson and Landis 2016; Mikelić et al. 2015; Miehe et al. 2015b; Zhou et al. 2019, 2018; Aldakheel et al. 2021; Heider and Markert 2017; Santillan et al. 2017; Bourdin et al. 2012; Wheeler et al. 2014; Mikelić et al. 2015; Lee et al. 2016c; Heider 2021; Lee et al. 2016b; Shiozawa et al. 2019). In many of these studies, the phase-field variable is used as an indicator function to distinguish between the surrounding medium and the fracture zone. Wheeler et al. (2020) built an integrated phase-field simulator for fluid-driven fracture propagation (IPACS), which coupled to reservoir simulators of phase-field models (Wick et al. 2016; Yoshioka and Bourdin 2016). Noii and Wick (2019) introduced a phase-field description for non-isothermal propagating fractures with a fixed temperature difference. Recent further extensions to THM (thermo-hydraulic-mechanical) phase-field in poro-elasticity are by Heider et al. (2018); Nguyen et al. (2023); Suh and Sun (2021) and Wang et al. (2023). Nguyen et al. (2023) provided an up-to-date overview of the current state-of-the-art (in Sect. 1.2).

In this work, we further extend our approach to THMC phase-field fracture, which, for the first time, combines mechanics, phase-field, pressure, temperature (THM), and chemical modules. The acid–rock reaction is the major topic in acid fracturing. Several studies have proven that acid–rock reaction would change rock strength and porosity over time (Hou et al. 2019; Guo et al. 2014; Luo et al. 2020). It offers challenges to the coupling system and other equations. We consider a prototype chemical equation combined with diffusion, transport and reaction terms and take the acid etching result into other equations. The overall algorithm is of iterative coupling type. From the engineering and numerical point of view, the acid area and fracture area are both important regions that need the small mesh size during the simulation. An effective way to satisfy local precision and global computation cost is adaptive mesh refinement of predictor–corrector type (Heister et al. 2015). In this work, it is extended by considering phase-field and acid concentration together in the mesh refinement indicators.

The outline of this paper is as follows: The governing equations are stated in Sect. 2. We take the interactions between multi-physical parameters into consideration. The energy functional and the related Euler–Lagrange equations were analyzed. The main algorithm is presented in Sect. 3. The adaptive predictor–corrector mesh refinement method is adopted and extended in this study. Several numerical examples are shown in Sect. 4 to prove the potential of this model for treating practical engineering. In Sect. 5. a difference function is defined based on the idea of the phase-field method, which can evaluate the accuracy and rightness of numerical simulation quantitatively. We believe that this

THMC coupling model can help engineers understand the process of acid fracturing better.

2 Modeling of acid fractures

Let $\Lambda \in \mathbb{R}^2$ be a smooth open and bounded computational domain with boundary $\partial\Lambda$. The computational time interval is $t \in [0, T]$ with the final time $T > 0$. First, we define the fracture f as a lower dimensional object which is contained compactly in Λ as shown in Fig. 1 (left). However, to consider a fracture f as a higher dimensional domain, we consider the phase-field approach, where the scalar-valued phase-field function is defined as $\phi : \Lambda \times [0, T] \to [0, 1]$. Here, $\phi = 0$ and $\phi = 1$ indicate a fracture and reservoir, respectively. The region $0 < \phi < 1$ implies the diffusive intermediate state with the thickness ε. More details are shown in Fig. 1. By utilizing the phase-field function, we divide the computational domain Λ implicitly into two sub-domains, namely fracture sub-domain ($\Omega_F(t)$) and reservoir sub-domain ($\Omega_R(t)$), i.e $\Lambda = \bar{\Omega}_F \cup \bar{\Omega}_R$. Then, we define the fracture interface $\partial F := \Gamma(t) := \Omega_F(t) \cap \Omega_R(t)$.

Moreover, there are four additional solution variables in this model, which include the vector-valued displacement $\mathbf{u} : \Lambda \times [0, T] \to \mathbb{R}^2$, the scalar-valued pressure $p : \Lambda \times [0, T] \to \mathbb{R}$, the scalar-valued temperature $\Theta : \Lambda \times [0, T] \to \mathbb{R}$, and the scalar-valued acid concentration $c : \Lambda \times [0, T] \to [0, 1]$. For each sub-domain, we have $p_F := p|_{\Omega_F}$, $p_R := p|_{\Omega_R}$, $\Theta_F := \Theta|_{\Omega_F}$, $\Theta_R := \Theta|_{\Omega_R}$, $c_F := c|_{\Omega_F}$, and $c_R := c|_{\Omega_R}$. Several physical variables interact with each other, and they have numerical lower and upper bounds on their values due to their mathematical structure, such as the phase field variable and the concentration of acid. In this model, the following assumptions are made:

1. The configuration is assumed to be isotropic and symmetric;
2. Fracture propagation is irreversible;
3. The rock strength under acid etching decreases monotonically and continuously;

4. The gas and heat produced by the acid–rock reaction have no influence on the system;
5. The acid fluid consists solely of hydrochloric acid;
6. All fractures and natural structures are filled with fluid;
7. The fluid is micro-compressible in this model.

Based on the notation and preliminary assumptions, the following five different modules are introduced: Temperature module, pressure module, chemical module for acid fracture, geomechanics (displacements) module, and phase-field fracture indicator function module. We notice that the last two are introduced directly in a coupled fashion since already well-known as basic phase-field fracture model; see the many references in the introduction. Moreover, not all possible nonlinear couplings are necessary between all different equations, and details will be discussed in each respective subsection.

2.1 Temperature equation for acid fractures

First, we introduce the temperature equation. It has been shown that reservoir temperature affects the heat transfer properties more strongly than fluid behavior (Shu et al. 2020; Xue et al. 2023). We assume that the fluid moves slowly enough such that inertia effects and the heat radiation can be neglected (Bai et al. 2017; Jiang et al. 2023). Then the temperature equation in two sub-domains (Ω_F and Ω_R) can be written as: Find $\Theta_F : \bar{\Omega}_F \times [0, T] \to \mathbb{R}$ and $\Theta_R : \bar{\Omega}_R \times [0, T] \to \mathbb{R}$ such that:

$$\frac{\partial}{\partial t}(\mathrm{Cap}_F \rho_F \Theta_F) = \nabla \cdot K_{Fd} \nabla \Theta_F - V_F \cdot \nabla \Theta_F + q_{F\Theta} \text{ in } \Omega_F(t) \times [0, T], \tag{1}$$

$$\frac{\partial}{\partial t}(\mathrm{Cap}_R \rho_R \Theta_R) = \nabla \cdot K_{Rd} \nabla \Theta_R - V_R \cdot \nabla \Theta_R + q_{R\Theta} \text{ in } \Omega_R(t) \times [0, T]. \tag{2}$$

Here, $\rho_F > 0$ and $\rho_R > 0$ are the densities of mixture of solid and fluid in the fracture and reservoir, respectively, where $\rho_R := \varphi_R^* \rho_{Rf} + (1 - \varphi_R^*)\rho_{Rr}$ and $\rho_F := \rho_{Ff}$. $\rho_{Rr} > 0$ is the rock density in the reservoir, $\varphi_R^* > 0$ is the porosity of the reservoir (defined in Eq. (5)). The fluid densities in fracture
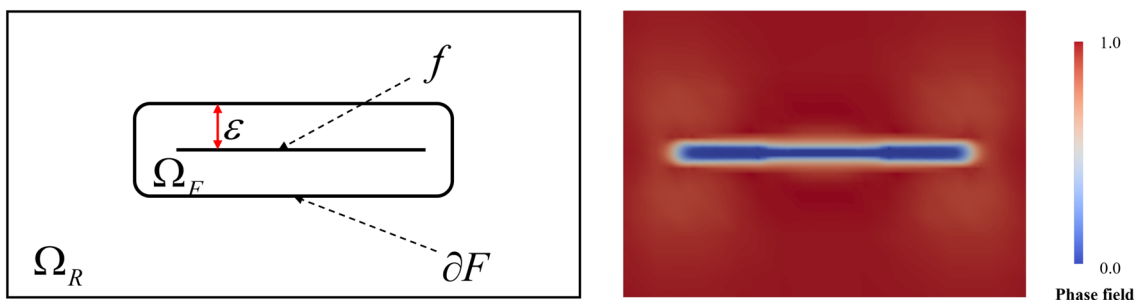

Fig. 1 The phase-field description for acid fracture using the function ϕ

ρ_{Ff} and reservoir ρ_{Rf} are defined in Eqs. (8) and (9). In addition, Cap_F, $\text{Cap}_R > 0$ are the heat capacities of the reservoir and the fracture, respectively, and K_{Fd}, $K_{Rd} > 0$ are the thermal diffusion coefficient of reservoir and fracture, respectively. Fluid velocities in the fracture V_F and in the reservoir V_R are defined in the Eq. (7), and the detailed expression for the source terms $q_{F\Theta}$ and $q_{R\Theta}$ will be given in Eq. (60). The initial and boundary conditions depend on the problem and are shown in the numerical examples section.

2.2 Pressure equation for acid fractures

The pressure module was first developed for fluid-filled phase-field fractures by Mikelić et al. (2015), which was modified with the indicator functions to enhance robustness (Lee et al. 2016c). Based on the mass continuity, the fluid equation can be written as:

$$\frac{\partial}{\partial t}\left(\rho_{Ff}\varphi_F^*\right) + \nabla \cdot \left(\rho_{Ff}V_F\right) = q_{Ff} - q_L \ \text{ in } \ \Omega_F(t) \times [0,T], \tag{3}$$

$$\frac{\partial}{\partial t}\left(\rho_{Rf}\varphi_R^*\right) + \nabla \cdot \left(\rho_{Rf}V_R\right) = q_{Rf} \ \text{ in } \ \Omega_R(t) \times [0,T], \tag{4}$$

where φ_F^* and φ_R^* are the porosities of reservoir and fracture respectively, where $\varphi_F^* = 1.0$ and

$$\varphi_R^* = \varphi_R^0 + \alpha\nabla \cdot \mathbf{u} + \frac{1}{M}(p - p_0) + K_{tc}(\Theta - \Theta_0) + A_{etch}(c). \tag{5}$$

Here, $0 < \varphi_R^0 < 1$ is the initial porosity of the reservoir, Θ_0 is the initial temperature, p_0 is the initial pressure, $\alpha \in [0,1]$ is the Biot coefficient, $M > 0$ is the Biot modulus, $K_{tc} > 0$ is the thermal expansion coefficient of pores. In addition, $A_{etch}(c)$ is the acid effect term, which is defined as

$$A_{etch}(c) := K_{etch}\int_0^{t_{etch}} R_c \, dt, \tag{6}$$

where $K_{etch} > 0$ is the acid etching coefficient, R_c is the reaction term which is defined in the following section (Eq. (15)), t_{etch} is the etching time at a fixed point. The source terms include the leak-off term (Mikelić et al. 2015; Lee et al. 2016c) q_L, and q_{Ff} and q_{Rf} are the fluid injection/production terms in the reservoir and fracture, respectively.

The velocities are given by Darcy's law as

$$V_i := -\frac{K_i}{\eta_i}\nabla p_i, \ i = F, R, \tag{7}$$

and, for the simplicity, we neglect the influence of gravity. Here, $\eta_F > 0$ and $\eta_R > 0$ are the fluid viscosities. K_F, $K_R \in \mathbb{R}^+$ are the permeabilities. The fluid is assumed to be compressible, where $K_{Ffc} \in \mathbb{R}^+$ and $K_{Rfc} \in \mathbb{R}^+$ are the fluid compressibilities. Then, we have:

$$\rho_{Ff} = \rho_{Ff}^0[1 + K_{Ffc}(p_F - p_F^0)], \tag{8}$$

$$\rho_{Rf} = \rho_{Rf}^0[1 + K_{Rfc}(p_R - p_R^0)], \tag{9}$$

by assuming that the K_{Ffc} and K_{Rfc} are small, and ρ_{Ff}^0 and ρ_{Rf}^0 are the initial fluid densities in fracture and reservoir.

Then, the pressure equation can be re-written as: Find $p_F : \bar{\Omega}_F \times [0,T] \to \mathbb{R}$ and $p_R : \bar{\Omega}_R \times [0,T] \to \mathbb{R}$ such that:

$$\rho_{Ff}^0 K_{Ffc}\partial_t(p_F) - \nabla \cdot \rho_{Ff}^0 \frac{K_F}{\eta_F}(\nabla p_F) = q_{Ff} - q_L, \quad \text{in } \Omega_F(t) \times [0,T], \tag{10}$$

$$\rho_{Rf}^0\partial_t\left(\alpha\nabla \cdot u + \frac{1}{M}p_R + K_{tc}\Theta_R + A_{etch}\right) \\ - \nabla \cdot \rho_{Rf}^0 \frac{K_R}{\eta_R}(\nabla p_R) = q_{Rf}, \quad \text{in } \Omega_R(t) \times [0,T]. \tag{11}$$

The boundary and initial conditions depend on the problem and are given in the numerical examples section.

2.3 Chemical equation for acid fractures

The acid fracturing fluid is based on hydrochloric acid, and the chemical reaction (Hou et al. 2021) is given by:

$$2HCl + CaCO_3 = CaCl_2 + H_2O + CO_2. \tag{12}$$
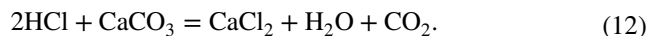
Here, the unknown variable is the hydrochloric acid concentration. The acid would be injected into the model and react with the rock, which adheres to the law of conservation of matter. The acid moves with the fluid and diffuses from regions of high concentration to those of low concentration. The acid–rock reaction takes place exclusively when the acid contacts with the rock, so there is no reaction term in Eq. (13). The acid–rock reaction rate is influenced by factors such as temperature, pressure, and acid concentration, which is later described in Eq. (16). Thus, the chemical equation for acid diffusion, transport, and reaction can be written as: Find the acid concentrations $c_F : \bar{\Omega}_F \times [0,T] \to \mathbb{R}$ and $c_R : \bar{\Omega}_R \times [0,T] \to \mathbb{R}$ such that:

$$\frac{\partial}{\partial t}\left(\varphi_F^* c_F\right) = K_{Fc}\nabla \cdot \left(\varphi_F^* c_F\right) - V_F \cdot \nabla c_F + q_{Fc} \ \text{ in } \Omega_F(t) \times [0,T], \tag{13}$$

$$\frac{\partial}{\partial t}\left(\varphi_R^* c_R\right) = K_{Rc}\nabla \cdot c_R - V_R \cdot \nabla c_R + q_{Rc} \\ - \varphi_R^* R_c \ \text{ in } \Omega_R(t) \times [0,T]. \tag{14}$$

The penalization method for the chemical equation is introduced in Sect. 3.4 since the acid solution should follow the physical limits. Here, K_{Fc}, $K_{Rc} > 0$ are the acid diffusion coefficients of the reservoir and fracture respectively, and q_{Fc}, q_{Rc} are the acid source terms. According to Eq. (12), the reaction term can be described as:

$$R_c := 2K_{ar}(p, \Theta)c_R{}^2, \tag{15}$$

where $K_{ar}(p, \Theta)$ is reaction rate speed, which is affected by pressure and temperature (Arrhenius 1889; Pham et al. 2022). In this paper, we set as:

$$K_{ar}(p, \Theta) := k_{ar}\left(\frac{p}{p_r}\right)^{-\frac{1}{2}} \exp\left(-\frac{Ea}{R\Theta_T}\right), \tag{16}$$

where $k_{ar} > 0$ is the reaction rate constant at a reference pressure, p_r is the reference pressure, Ea is the activation energy of Eq. (12), $R > 0$ is the gas constant, and Θ_T is the absolute temperature.

2.4 The Phase-Field Energy Functional for Acid Fracture

The phase-field fracture system consists of a displacement variable **u** describing geomechanics and a phase-field indicator function ϕ describing the fracture. Traditionally, this was introduced from an energy point of view (Francfort and Marigo 1998; Bourdin et al. 2000) and later interpreted as a thermodynamically consistent phase-field model (Kuhn and Müller 2010; Miehe et al. 2010). The energy equation for variational fracture (yet without ϕ) can be described as:

$$E(\mathbf{u}, f) = \frac{1}{2}\int_{\Omega} \sigma(\mathbf{u}) : e(\mathbf{u}) \, d\mathbf{x} + G_F H^{d-1}(f), \tag{17}$$

where, $\Omega = \Lambda \backslash f$, $G_F > 0$ is the critical energy release rate, and $H^{d-1}(f)$ is the length of the fracture. The linear elastic stress tensor ($\sigma(\mathbf{u})$) and strain tensor ($e(\mathbf{u})$) are described as:

$$\sigma(\mathbf{u}) = \lambda(\nabla \cdot \mathbf{u})I + 2Ge(\mathbf{u}), \quad e(\mathbf{u}) = \frac{\nabla\mathbf{u} + \nabla\mathbf{u}^T}{2}, \tag{18}$$

where, $\lambda, G > 0$ are the Lamé coefficients, and I is the identity tensor. In this model, we assume that the acid fracture would begin in the homogeneous media and the rock parameter would change with the acid etching. Thus, the acid fracturing problem becomes a dynamic heterogeneous problem. It is well known from the previous studies (Pournik 2008; Melendez et al. 2007; Zhou et al. 2021), that different rock samples would lead to different trends in the change of rock strength after acid etching. Here, we assume that the rock strength under acid etching decreases monotonically and continuously and the mechanical parameters would change as:

$$E = E_0 - K_{Eetch}\int_0^{t_{etch}} R_c dt \, , \, v = v_0. \tag{19}$$

Here, $K_{Eetch} > 0$ is the acid effect constant for Young's modulus. E is the Young's modulus and v is the Poisson ratio. E_0 and v_0 are the initial Young's modulus and initial Poisson ratio. According to Hooke's Law, the lame coefficients λ, G are defined as:

$$G = \frac{E}{2(1 + v)} \, , \, \lambda = \frac{Ev}{(1 + v)(1 - 2v)}. \tag{20}$$

Thus, we can rewrite the Eq. (18):

$$\sigma(\mathbf{u}, c) := \lambda(c, t)(\nabla \cdot \mathbf{u})I + 2G(c, t)e(\mathbf{u}). \tag{21}$$

In the following, we perform two modifications in Eq. (17). First, the poroelastic stress tensor $\sigma_{eff} := \sigma(\mathbf{u}, c) - \alpha pI$ contributes one additional term, namely αpI. Here, $\alpha \in [0, 1]$ is Biot's coefficient. The same procedure applies to the temperature contribution. Coussy (2004) proposed the resulting free-energy model. The use of these ideas for fracture formulations in porous media was outlined by Tran et al. (2013). The extension to phase-field fracture descriptions in pressurized and non-isothermal configurations was derived by Noii and Wick (2019). To this end, we obtain the energy functional

$$E(\mathbf{u}, p, c, \Theta, f) = \frac{1}{2}\int_{\Omega} \sigma(\mathbf{u}, c) : e(\mathbf{u})d\mathbf{x} - \int_{\Omega} \alpha p\nabla \cdot \mathbf{u} \, d\mathbf{x}$$
$$- \int_{\Omega} 3\alpha_{\Theta}K_d\Theta\nabla \cdot \mathbf{u} \, d\mathbf{x} + G_F H^{d-1}(f). \tag{22}$$

Here, $3\alpha_{\Theta} > 0$ is the thermal expansion coefficient and $K_d := G + \lambda$. The first three terms in the above equation are bulk energy terms and $G_F H^{d-1}(f)$ is the fracture surface energy term. The latter can be rewritten as a computable form by utilizing the phase-field by employing the following Ambrosio–Tortorelli elliptic functional approximation (Ambrosio and Tortorelli 1990, 1992; Bourdin et al. 2000). In more detail, the line integral $G_F H^{d-1}(f)$ is difficult to approximate numerically. Thus, the elliptic approximation is defined as domain integral and makes it easier to treat numerically. To this end, we work with

$$\int_f G_F ds \approx \int_{\Lambda} G_F\left(\frac{1}{2\varepsilon}(1 - \phi)^2 + \frac{\varepsilon}{2}(\nabla\phi)^2\right) d\mathbf{x}. \tag{23}$$

Inserting (23) into (22) yields

$$E(\mathbf{u}, p, c, \Theta, f) = \frac{1}{2}\int_{\Omega} \sigma(\mathbf{u}, c) : e(\mathbf{u})d\mathbf{x} - \int_{\Omega} \alpha p\nabla \cdot \mathbf{u} \, d\mathbf{x}$$
$$- \int_{\Omega} 3\alpha_{\Theta}K_d\Theta\nabla \cdot \mathbf{u} \, d\mathbf{x} + \int_{\Lambda} G_F\left(\frac{1}{2\varepsilon}(1 - \phi)^2 + \frac{\varepsilon}{2}(\nabla\phi)^2\right) d\mathbf{x}. \tag{24}$$

In this energy functional, porous media contributions and phase-field of the reservoir are included. However, the specific influence of the fracture itself is not yet contained. Utilizing interface laws of continuity of pressures and temperatures, as well as continuity of the stress tensors into

normal directions, were performed by Noii and Wick (2019). These ideas were earlier derived and discussed by Mikelić et al. (2013); Wick (2020). Numerical approximation of interface laws becomes challenging due to the smeared representation of fractures with only the phase field. Mikelić et al. (2013) employed Gauss' divergence theorem to rewrite interface contributions as domain integrals. With two new contributions for both the pressure and the temperature in Eq. (23), the energy functional for acid fracture can be written as:

$$
\begin{aligned}
E(\mathbf{u}, p, c, \Theta, \phi) =& \int_\Lambda \frac{1}{2}((1-k)\phi^2 + k)\sigma^+(\mathbf{u}, c) : e(\mathbf{u})d\mathbf{x} + \int_\Lambda \frac{1}{2}\sigma^-(\mathbf{u}, c) : e(\mathbf{u})d\mathbf{x} \\
& - \int_\Lambda (\alpha - 1)\phi^2 p \nabla \cdot \mathbf{u}\, d\mathbf{x} + \int_\Lambda (\phi^2 \nabla p)\mathbf{u}\, d\mathbf{x} \\
& - \int_\Lambda (3\alpha_\Theta K_d + C_\Theta)\phi^2 \Theta \nabla \cdot \mathbf{u}\, d\mathbf{x} + \int_\Lambda C_\Theta \phi^2 \nabla \Theta \mathbf{u}\, d\mathbf{x} \\
& + \int_\Lambda G_F \left(\frac{1}{2\varepsilon}(1-\phi)^2 + \frac{\varepsilon}{2}(\nabla \phi)^2 \right) d\mathbf{x},
\end{aligned}
\tag{25}
$$

Here, k is a positive regularization parameter for the elastic energy and C_Θ is a constant to describe the relation for the temperature near the fracture (Tran et al. 2013). Due to the irreversibility constraint and loading conditions, phase-field fracture is an incremental or time-dependent procedure. Here and above, we consider a quasi-static setting in which no time derivatives appear in the main equations, but only in the irreversibility constraint. However, this means that the variables are space and time-dependent. Then, let p, Θ, c be given, find $\mathbf{u} : \Lambda \times [0, T] \to \mathbb{R}^2$, $\phi : \Lambda \times [0, T] \to [0, 1]$ through the complementarity system

$$
\begin{aligned}
-\nabla \cdot (((1-k)\phi^2 + k)\sigma^+(\mathbf{u}, c) + \sigma^-(\mathbf{u}, c)) + (\alpha - 1)\nabla(\phi^2 p) \\
+ \phi^2 \nabla p + (3\alpha_\Theta K_d + C_\Theta)\nabla(\phi^2 \Theta) + \phi^2 \nabla \Theta = 0 \quad \text{in } \Lambda \times [0, T],
\end{aligned}
\tag{26}
$$

$$
\begin{aligned}
-((1-k)\sigma^+ : e(\mathbf{u})\phi - \frac{G_F}{\varepsilon}(1-\phi) - G_F \varepsilon \Delta \phi - 2(\alpha - 1)\phi p \nabla \cdot \mathbf{u} \\
+ 2\phi \nabla p \mathbf{u} - 2(3\alpha_\Theta K_d + C_\Theta)\phi \Theta \nabla \cdot \mathbf{u} + 2C_\Theta \phi \nabla \Theta \mathbf{u}) \le 0 \quad \text{in } \Lambda \times [0, T],
\end{aligned}
\tag{27}
$$

$$
\partial_t \phi \le 0 \quad \text{in } \Lambda \times [0, T],
\tag{28}
$$

$$
\begin{aligned}
-((1-k)\sigma^+ : e(\mathbf{u})\phi - \frac{G_F}{\varepsilon}(1-\phi) - G_F \varepsilon \Delta \phi - 2(\alpha - 1)\phi p \nabla \cdot \mathbf{u} \\
+ 2\phi \nabla p \mathbf{u} - 2(3\alpha_\Theta K_d + C_\Theta)\phi \Theta \nabla \cdot \mathbf{u} + 2C_\Theta \phi \nabla \Theta \mathbf{u})\partial_t \phi = 0 \quad \text{in } \Lambda \times [0, T].
\end{aligned}
\tag{29}
$$

2.5 Initial and Boundary Conditions

In this section, we supplement the initial and boundary conditions in the system. The acid fractures begin at a homogeneous media. For all $x \in \Omega_F \cup \Omega_R(t = 0)$, p_F^0, p_R^0 are the smooth given pressure. Θ_F^0, Θ_R^0 are the smooth given temperature. c_F^0, c_R^0 are the smooth given acid concentration. We also have $\phi(x, 0) = \phi^0$, where ϕ^0 is the given initial phase-field. We prescribe Dirichlet boundary conditions for temperature, pressure, displacement and acid equation on $\partial \Lambda$. The boundary conditions for this model are given as follows:

$$
\mathbf{u} = 0, \ \partial_n \phi = 0, \ p = f_p, \ \Theta = f_\Theta, \ c = f_c \quad \text{on } \partial \Lambda \times [0, T],
\tag{30}
$$

Here, n is the outward normal vector of the domain Λ, and f_p, f_Θ, f_c are the given boundary values.

3 Numerical Modeling, Discretization and Solution Algorithms

In this section, we discuss numerical aspects of the previously defined systems. First, numerical discretizations in time and space are introduced for each module. The final goal is the design of an algorithm that couples all modules.

The strong forms need to be rewritten into weak formulations (Lee et al. 2016c, 2017a; Wheeler et al. 2020), which our overall numerical modeling strategy relies on. Here, care must be taken for the mechanics-phase-field part since the phase-field function is subject to a fracture irreversibility constraint. The governing functional framework is posed in function spaces and convex sets, forming a CVIS (coupled variational inequality system). In this work, this is regularized by using a primal-dual active set method for a primal-dual active set phase-field formulation (Heister et al. 2015). Then, temporal and spatial discretizations are applied.

Next, indicator variables obtained from the phase-field functions are computed for the three diffraction systems, namely pressure, temperature, and chemical equation. Having all weak forms at hand, a final algorithm based on the fixed-stress scheme will be derived. Here, we extend our own previously derived algorithms (Lee et al. 2017a) to the THMC phase-field fracture system.

3.1 Discretization: Basics

A mesh family $\{M_h\}_{h>0}$ is introduced and assumed to be shape regular. Each mesh M_h is square and a subdivision of $\overline{\Lambda}$ made of disjoint elements $\mathcal{K}$. Each subdivision is assumed to approximate the computational domain. The diameter of an element $\mathcal{K} \in M_h$ is denoted by h, and h_{max} is the global refine mesh size and h_{min} is the local refine mesh size. The computational time interval ($[0, T]$) is discretized as $0 := t^0 < \cdots < t^n < \cdots < t^N := T$. The time step size is $\delta t := t^n - t^{n-1}$. The domain Λ is divided into the fracture sub-domain ($\Omega_F(t)$) and reservoir sub-domain ($\Omega_R(t)$). Here we introduce the indicator functions:

$$\chi_F(x,t) := \begin{cases} 1 & \text{if } \phi < D_f, \\ 1 - \phi(x,t) & \text{if } D_f < \phi < D_r, \\ 0 & \text{if } \phi > D_r, \end{cases}$$
$$\chi_R(x,t) := \begin{cases} 1 & \text{if } \phi < D_f \\ \phi(x,t) & \text{if } D_f < \phi < D_r . \\ 0 & \text{if } \phi > D_r \end{cases} \tag{31}$$

Thus, $\chi_F(x, t) = 1$ in fracture sub-domain and $\chi_R(x, t) = 1$ in reservoir sub-domain. It follows $\chi_F + \chi_R = 1$ obviously. Here, $0 < D_f < D_r < 1$ are the distinguishing indexes for fracture and reservoir. The indicator functions are continuous in the intermediate state.

3.2 Discretization of the Temperature Equation

Since the fluid compressibility is small enough, the temperature equation for both fracture and reservoir subdomains can be rewritten as:

$$\text{Cap}_F \rho_{Ff}^0 \frac{\partial \Theta_F}{\partial t} = \nabla \cdot K_{Fd} \nabla \Theta_F - V_F \cdot \nabla \Theta_F + q_{F\Theta} \quad \text{in } \Omega_F(t) \times [0, T], \tag{32}$$

$$\text{Cap}_R \rho_{Rr} \frac{\partial \Theta_R}{\partial t} + \text{Cap}_R (\rho_{Rf}^0 - \rho_{Rr}) \frac{\partial \varphi_R^* \Theta_R}{\partial t}$$
$$= \nabla \cdot K_{Rd} \nabla \Theta_R - V_R \cdot \nabla \Theta_R + q_{R\Theta} \quad \text{in } \Omega_R(t) \times [0, T]. \tag{33}$$

The space approximation Θ of the temperature is approximated by using continuous piecewise polynomials given in the finite element space $\mathbb{W}(M_h)$. According to the Galerkin method, the temperature equation can be discretized as:

$$\chi_F(\cdot, \phi) \left(\int_\Lambda \left(\text{Cap}_F \rho_{Ff}^0 \frac{\partial \Theta}{\partial t} \right) \omega d\mathbf{x} = \int_\Lambda \nabla \cdot K_{Fd} \nabla \Theta \omega d\mathbf{x} \right.$$
$$\left. - \int_\Lambda V_F \cdot \nabla \Theta \omega d\mathbf{x} + \int_\Lambda q_{F\Theta} \omega d\mathbf{x} \right), \tag{34}$$

$$\chi_R(\cdot, \phi) \left(\int_\Lambda \left(\text{Cap}_R \rho_{Rr} \frac{\partial \Theta}{\partial t} + \text{Cap}_R (\rho_{Rf}^0 - \rho_{Rr}) \frac{\partial \varphi_R^* \Theta}{\partial t} \right) \omega d\mathbf{x} \right.$$
$$= \int_\Lambda \nabla \cdot K_{Rd} \nabla \Theta \omega d\mathbf{x} \tag{35}$$
$$\left. - \int_\Lambda V_R \cdot \nabla \Theta \omega d\mathbf{x} + \int_\Lambda q_{R\Theta} \omega d\mathbf{x} \right), \quad \forall \omega \in \mathbb{W}(M_h).$$

Then we discretize the equation in time by utilizing the first order backward Euler method. Let the ϕ^n, p^n and Θ^n be given, then Θ^{n+1} can be computed as:

$$B_{F\Theta}(\Theta^{n+1})(\omega) = \chi_F(\cdot, \phi^n) \left(\int_\Lambda \left(\text{Cap}_F \rho_{Ff}^0 \frac{\Theta^{n+1} - \Theta^n}{\delta t} \right) \omega d\mathbf{x} \right.$$
$$+ - \int_\Lambda \nabla \cdot K_{Fd} \nabla \Theta^{n+1} \omega d\mathbf{x} \tag{36}$$
$$\left. + \int_\Lambda V_F^n \cdot \nabla \Theta^{n+1} \omega d\mathbf{x} - \int_\Lambda q_{F\Theta} \omega d\mathbf{x} \right),$$

$$B_{R\Theta}(\Theta^{n+1})(\omega)$$
$$= \chi_R(\cdot, \phi^n) \left(\int_\Lambda \left(\text{Cap}_R \left(\varphi_R^0 \rho_{Rf}^0 + (1 - \varphi_R^0) \rho_{Rr} \right) \frac{\Theta^{n+1} - \Theta^n}{\delta t} \right) \omega d\mathbf{x} \right.$$
$$\left. - \int_\Lambda \nabla \cdot K_{Rd} \nabla \Theta^{n+1} \omega d\mathbf{x} + \int_\Lambda V_R^n \cdot \nabla \Theta^{n+1} \omega d\mathbf{x} - \int_\Lambda q_{R\Theta} \omega d\mathbf{x} \right), \tag{37}$$

$$B_\Theta(\Theta^{n+1})(\omega) = B_{F\Theta}(\Theta^{n+1})(\omega) + B_{R\Theta}(\Theta^{n+1})(\omega) = 0. \tag{38}$$

3.3 Discretization of the Pressure Equation

The space approximation P of the pressure is approximated by using continuous piecewise polynomials given in the finite element space, $\mathbb{W}(M_h)$. According to the Galerkin method, the pressure equation can be discretized as:

$$\chi_F(\cdot, \phi) \left(\int_\Lambda \left(\rho_{Ff}^0 K_{Ffc} \partial_t P \right) \omega d\mathbf{x} \right.$$
$$\left. - \int_\Lambda \left(\rho_{Ff}^0 \frac{K_F}{\eta_F} (\nabla P) \right) \nabla \omega d\mathbf{x} = \int_\Lambda (q_{Ff} - q_L) \omega d\mathbf{x} \right), \tag{39}$$

$$\chi_R(\cdot, \phi) \left(\int_\Lambda \left(\rho_{Rf}^0 \partial_t \left(\alpha \nabla \cdot u + \frac{1}{M} P + K_{tc} \Theta_R + A_{etch} \right) \right) \omega d\mathbf{x} \right.$$
$$\left. - \int_\Lambda \left(\rho_{Rf}^0 \frac{K_R}{\eta_R} (\nabla P) \right) \nabla \omega d\mathbf{x} = \int_\Lambda q_{Rf} \omega d\mathbf{x} \right), \quad \forall \omega \in \mathbb{W}(M_h). \tag{40}$$

Then we discretize the equation in time by utilizing the first order backward Euler method. Let the $\Theta^{n+1}, \Theta^n, \mathbf{u}^{n+1}, \mathbf{u}^n, c^n, c^{n-1}$ and P^n be given, then the P^{n+1} can be computed as:

$$
\begin{aligned}
B_{Fp}(P^{n+1})(\omega) = \chi_F(\cdot, \phi^n)\bigg(&\int_\Lambda \left(\rho_{Ff}^0 K_{Ffc} \frac{P^{n+1} - P^n}{\delta t} \right) \omega d\mathbf{x} \\
&- \int_\Lambda \left(\rho_{Ff}^0 \frac{K_F}{\eta_F} \nabla P^{n+1} \right) \nabla \omega d\mathbf{x} \\
&- \int_\Lambda (q_{Ff} - q_L) \omega d\mathbf{x} \bigg),
\end{aligned}
\tag{41}
$$

$$
\begin{aligned}
&B_{Rp}(P^{n+1})(\omega) \\
&= \chi_R(\cdot, \phi^n)\bigg(\int_\Lambda \rho_{Rf}^0 \bigg(\alpha \frac{\nabla \cdot u^{n+1} - \nabla \cdot u^n}{\delta t} + \frac{1}{M} \frac{P^{n+1} - P^n}{\delta t} \\
&\quad + K_{tc} \frac{\Theta^{n+1} - \Theta^n}{\delta t} + \frac{A_{etch}^n - A_{etch}^{n-1}}{\delta t} \bigg) \omega d\mathbf{x} \\
&\quad - \int_\Lambda \left(\rho_{Rf}^0 \frac{K_R}{\eta_R} \nabla P^{n+1} \right) \nabla \omega d\mathbf{x} - \int_\Lambda q_{Rf} \omega d\mathbf{x} \bigg),
\end{aligned}
\tag{42}
$$

$$
B_P(P^{n+1})(\omega) = B_{Fp}(P^{n+1})(\omega) + B_{Rp}(P^{n+1})(\omega) = 0.
\tag{43}
$$

Here, the pressure source term is given with the leak-off term q_L, which is defined as (Heister et al. 2015):

$$
q_L := \nabla \cdot (\rho_{Ff} V_{leak}).
\tag{44}
$$

3.4 Discretization of the Chemical Equation with Penalization Method

The chemical equation for acid fractures and reservoir subdomains can be written as:

$$
\partial_t c_F = K_{Fc} \nabla \cdot c_F - V_F \cdot \nabla c_F + q_{Fc} \quad \text{in } \Omega_F(t) \times [0, T],
\tag{45}
$$

$$
\begin{aligned}
\partial_t \left(\varphi_R^* c_R \right) = &K_{Rc} \nabla \cdot c_R - V_R \cdot \nabla c_R \\
&+ q_{Rc} - \varphi_R^* R_c \left(c_R^{n-1}, p_R^{n-1}, \Theta_R^{n-1} \right) \quad \text{in } \Omega_R(t) \times [0, T].
\end{aligned}
\tag{46}
$$

Here, R_c is a chemical reaction coupling term, and for the simplicity, we linearize it by employing the old timestep solutions of acid, temperature, and pressure. In addition, the acid injection terms are related to fluid rate, pressure and temperature (Eqs. (64), (65)).

Due to the physical meaning of hydrochloric acid content, the solution variable c_i in the chemical equation should follow $0 < c_i < c_s$ ($i = F$ in fracture domain and $i = R$ in reservoir domain), where c_s is the saturation concentration of acid, $c_s < 1$. Thus, to preserve this physics, the following penalization method is introduced in this model:

$$
\gamma_0[-c_i]^+ + \gamma_s[c_i - c_s]^+.
\tag{47}
$$

Therefore, we can rewrite the chemical equations with penalization as,

$$
\partial_t(c_F) + \gamma_0^+ + \gamma_s^+ = K_{Fc} \nabla \cdot (c_F) - V_F \cdot \nabla c_F + q_{Fc} \quad \text{in } \Omega_F(t) \times [0, T],
\tag{48}
$$

$$
\begin{aligned}
\partial_t \left(\varphi_R^* c_R \right) + \gamma_0^+ + \gamma_s^+ = &K_{Rc} \nabla \cdot c_R - V_R \cdot \nabla c_R \\
&+ q_{Rc} - \varphi_R^* R_c^{n-1} \quad \text{in } \Omega_R(t) \times [0, T].
\end{aligned}
\tag{49}
$$

If γ is too small, the penalization would have no effect, whereas if γ is too big will lead to ill-conditioned Jacobians and higher nonlinearities. Here we set:

$$
\gamma_0[-c_i]^+ = \begin{cases} 0 & \text{if } c_i > 0 \\ 0.1 & \text{if } c_i < 0 \end{cases}, \quad \gamma_s[c_i - c_s]^+ = \begin{cases} 0 & \text{if } c_i < c_s \\ 0.1 & \text{if } c_i > c_s \end{cases}.
\tag{50}
$$

The space approximation $C \in \mathbb{W}(M_h)$ of the acid concentration is approximated by using continuous piecewise polynomials given in the finite element space. Let the $\Theta^{n+1}, \Theta^n, \mathbf{u}^{n+1}, \mathbf{u}^n, P^{n+1}, P^n$ and C^n be given. The global C^{n+1} can be computed as:

$$
\begin{aligned}
B_{Fc}(C^{n+1})(\omega) = \chi_F(\cdot, \phi^n)\bigg(&\int_\Lambda \left(\frac{C^{n+1} - C^n}{\delta t} + (\gamma_0^+ + \gamma_s^+, C^n) \right) \omega d\mathbf{x} \\
&- \int_\Lambda (K_{Fc} \nabla \cdot C^{n+1} - V_F \cdot \nabla C^{n+1}) \omega d\mathbf{x} - \int_\Lambda q_{Fc} \omega d\mathbf{x}, \bigg)
\end{aligned}
\tag{51}
$$

$$
\begin{aligned}
B_{Rc}(C^{n+1})(\omega) = \chi_R(\cdot, \phi^n)\bigg(&\int_\Lambda (\varphi_R^* \frac{C^{n+1} - C^n}{\delta t} + (\gamma_0^+ + \gamma_s^+, C^n)) \omega d\mathbf{x} \\
&- \int_\Lambda (K_{Rc} \nabla \cdot C^{n+1} - V_R \cdot \nabla C^{n+1}) \omega d\mathbf{x} \\
&- \int_\Lambda (q_{Rc} - \varphi_R^* R_c^n) \omega d\mathbf{x} \bigg),
\end{aligned}
\tag{52}
$$

$$
B_c(C^{n+1})(\omega) = B_{Fc}(C^{n+1})(\omega) + B_{Rc}(C^{n+1})(\omega), \quad \forall \omega \in \mathbb{W}(M_h).
\tag{53}
$$

3.5 A Quasi-Monolithic Formulation of the Coupled Displacement Phase-Field System

In this section, we present a fully-coupled Euler–Lagrange formulation with a quasi-monolithic scheme for $\mathbf{U}$ and Φ (approximating $\mathbf{u}, \phi$) (Lee et al. 2016c). Therein, as proposed by Heister et al. (2015), the phase-field variable is linearized through an extrapolation $\tilde{\Phi}$ in the first term to obtain a robust numerical scheme. Let the initial conditions $p^0, \Theta^0, \mathbf{u}^0, \phi^0$ be given, and P^n, Θ^n are solution variables from the pressure equation and the temperature equation in time step n. Then, we seek $\{\mathbf{U}^{n+1}, \Phi^{n+1}\}$

$$A\big(\mathbf{U}^{n+1}, \Phi^{n+1}\big)\big(\mathbf{w}, \psi - \Phi^{n+1}\big)$$

$$= \int_\Lambda \big((1-k)\big(\tilde{\Phi}^{n+1}\big)^2 + k\big)\sigma^+(\mathbf{U}^{n+1}):e(\mathbf{w})d\mathbf{x} + \int_\Lambda \sigma^-(\mathbf{U}^{n+1}):e(\mathbf{w})d\mathbf{x}$$

$$- \int_\Lambda (\alpha - 1)\big(\Phi^{n+1}\big)^2 P^{n+1} \nabla \cdot \mathbf{w}d\mathbf{x} + \int_\Lambda \big(\Phi^{n+1}\big)^2 \nabla P^{n+1} \cdot \mathbf{w}d\mathbf{x}$$

$$- \int_\Lambda (3\alpha_\Theta K_d + C_\Theta)\big(\Phi^{n+1}\big)^2 \Theta^{n+1} \nabla \cdot \mathbf{w}d\mathbf{x}$$

$$- \int_\Lambda 2(\alpha - 1)\Phi^{n+1} P^{n+1} \nabla \cdot \mathbf{U}^{n+1} \cdot \big(\psi - \Phi^{n+1}\big)d\mathbf{x}$$

$$+ \int_\Lambda 2\Phi^{n+1} \nabla P^{n+1} \cdot \mathbf{U}^{n+1} \cdot \big(\psi - \Phi^{n+1}\big)d\mathbf{x} \qquad (54)$$

$$- \int_\Lambda 2(3\alpha_\Theta K_d + C_\Theta)\Phi^{n+1} \Theta^{n+1} \nabla \cdot \mathbf{U}^{n+1} \cdot \big(\psi - \Phi^{n+1}\big)d\mathbf{x}$$

$$+ \int_\Lambda 2C_\Theta \Phi^{n+1} \nabla\Theta^{n+1} \cdot \mathbf{U}^{n+1} \cdot \big(\psi - \Phi^{n+1}\big)d\mathbf{x}$$

$$- G_F \int_\Lambda \frac{1}{\varepsilon}\big(1 - \Phi^{n+1}\big) \cdot \big(\psi - \Phi^{n+1}\big)d\mathbf{x}$$

$$+ G_F \int_\Lambda \varepsilon \nabla\Phi^{n+1} \cdot \nabla\big(\psi - \Phi^{n+1}\big)d\mathbf{x} \geq 0.$$

The fixed-stress iteration method (Lee et al. 2017a; Mikelić and Wheeler 2012) is utilized to couple between pressure and displacement phase-field equations. Thus, for each time t^{n+1}, let $P^n, \mathbf{U}^n, \Phi^n$ be given, and we compute for $P^{l+1}, \mathbf{U}^{l+1}, \Phi^{l+1}$ in each iteration for $l = 0, 1, 2, \cdots$:

$$[B_P(P^{n+1})(\omega)]^{l+1} = [B_{Fp}(P^{n+1})(\omega)]^{l+1} + [B_{Rp}(P^{n+1})(\omega)]^{l+1} = 0, \qquad (55)$$

$$A\big(\mathbf{U}^{l+1}, \Phi^{l+1}\big)(\mathbf{w}, \psi)$$

$$= \int_\Lambda \big((1-k)\big(\tilde{\Phi}^{l+1}\big)^2 + k\big)\sigma^+(\mathbf{U}^{l+1}):e(\mathbf{w})d\mathbf{x} + \int_\Lambda \sigma^-(\mathbf{U}^{l+1}):e(\mathbf{w})d\mathbf{x}$$

$$- \int_\Lambda (\alpha - 1)\big(\Phi^{l+1}\big)^2 P^{l+1} \nabla \cdot \mathbf{w}d\mathbf{x} + \int_\Omega \big(\Phi^{l+1}\big)^2 \nabla P^{l+1} \cdot \mathbf{w}d\mathbf{x}$$

$$- \int_\Lambda (3\alpha_\Theta K_d + C_\Theta)\big(\Phi^{l+1}\big)^2 \Theta^{n+1} \nabla \cdot \mathbf{w}d\mathbf{x} + \int_\Lambda C_\Theta\big(\Phi^{l+1}\big)^2 \nabla\Theta^{n+1} \cdot \mathbf{w}d\mathbf{x}$$

$$+ \int_\Lambda (1-k)\Phi^{l+1}\sigma^+(\mathbf{U}^{l+1}):e(\mathbf{U}^{l+1}) \cdot \psi d\mathbf{x}$$

$$- \int_\Lambda 2(\alpha - 1)\Phi^{l+1} P^{l+1} \nabla \cdot \mathbf{U}^{l+1} \cdot \psi d\mathbf{x} \qquad (56)$$

$$+ \int_\Lambda 2\Phi^{l+1} \nabla P^{l+1} \cdot \mathbf{U}^{l+1} \cdot \psi d\mathbf{x}$$

$$- \int_\Lambda 2(3\alpha_\Theta K_d + C_\Theta)\Phi^{l+1} \Theta^{n+1} \nabla \cdot \mathbf{U}^{n+1} \cdot \psi d\mathbf{x}$$

$$+ \int_\Lambda 2C_\Theta \Phi^{l+1} \nabla\Theta^{n+1} \cdot \mathbf{U}^{l+1} \cdot \psi d\mathbf{x} - G_F \int_\Lambda \frac{1}{\varepsilon}\big(1 - \Phi^{n+1}\big) \cdot \psi d\mathbf{x}$$

$$+ G_F \int_\Lambda \varepsilon \nabla\Phi^{n+1} \cdot \nabla\psi d\mathbf{x} \geq 0.$$

The iteration would be completed if:

$$\max\{||\mathbf{U}^{l+1} - U^l||, ||\Phi^{l+1} - \Phi^l||, ||P^{l+1} - P^l||\} < TOL_{fs}, \ TOL_{fs} > 0. \qquad (57)$$

Then we set $\mathbf{U}^{n+1} = U^{l+1}, \Phi^{n+1} = \Phi^{l+1}, P^{n+1} = P^{l+1}$.

3.6 Adaptive Mesh Refinement Using a Predictor–Corrector Scheme

An important parameter in phase-field methods is the mesh size (h), which remains fixed during the simulation process. To maintain fracture resolution, it is necessary to ensure that $\varepsilon > h$. However, using a smaller mesh size will increase the demand for computational resources and result in longer computation times. Local mesh refinement is a popular method that allows us to refine only the regions of interest. When applied to fracture propagation problems, researchers must predict and refine the potential fracture propagation areas. Unfortunately, this method performs poorly in complex reservoirs due to the randomness of fracture propagation.

In multi-physics fracture propagation problems, a small mesh size is not only essential for improving numerical accuracy but also for obtaining better results and a more accurate representation of other physical parameters. The predictor–corrector adaptivity mesh refinement, as described by Heister et al. (2015), has been developed (Fig. 2). In this paper, we extend the adaptive mesh refinement technology to refine the mesh based on thresholds of the phase-field solution and the acid concentration together as

$$\phi(x) < TH_\phi \ \text{ or } \ c(x) > TH_c. \qquad (58)$$

Here, TH_ϕ and TH_c are the thresholds of the phase-field solution and the acid concentration. The algorithm is as follows:

Algorithm 1 Adaptive predictor-corrector mesh refinement with phase-field and acid indicators
---
1: Given the global refinement mesh size, local refinement mesh size, and the maximum number of refine times;
2: Predicate the fracture shape and other solution variables by solving once the system at global refine mesh size;
3: Refine the mesh in marked regions based on the thresholds;
4: Interpolate the old timestep solution variables in the refined mesh system and solve the system again;
5: Repeat steps 2-4 until the local refine mesh size or the maximum number of refine times are reached.

Despite solving the system several times, the effectiveness of this method has been proven (Heister et al. 2015).

Acid fracture propagation is a dynamic and heterogeneous process. We have extended the adaptive mesh refinement method by incorporating thresholds. The effectiveness of this approach is demonstrated in Fig. 3 and Sect. 4.1.

3.7 Final Algorithm for the Coupled THMC Phase-Field System

In our proposed THMC phase-field model developed in the previous sections, several partial differential equations and a variational inequality are coupled and need to be solved. Partitioned schemes and monolithic schemes are two basic approaches for solving this system. In the partitioned scheme, the equations are often solved separately, while in the monolithic coupling, the coupled equation system is solved as a whole. The governing equations in this paper are based on continuum mechanics and involve four physical fields and several physical quantities.

Our main algorithm is inspired from Wheeler et al. (2020), but adapted to our current system and the couplings with the relationship between the various physical quantities outlined in Fig. 4. We notice that not all equations couple, which is due to our assumptions made in Sect. 2, on the other hand, we are not aware even of a simplified (not all couplings are taken into account) THMC phase-field system published so far in the literature. A rigorous numerical and computational analysis of Algorithm 2 remains ongoing research.

The acid–rock reaction term affects the pressure equation, displacements-phase-field equation, and acid equation. Due to the continuity of the variables, this term is fixed with the solution variables at timestep t^n. We define $Res(\cdot)$ as the residual of each PDE system, where TOL_s represents the solver tolerance, with $\text{TOL}_s > 0$.

---

Algorithm 2 Solving algorithm for THMC coupling system
___
1: At timestep t^{n+1}, given P^n, Θ^n, C^n and get acid reaction term R_c^n
2: **repeat**
3:     Given Φ^n, Θ^n, P^n and R_c^n , find Θ^{n+1};
4:     Given $P^n, \Theta^{n+1}, \Theta^n, \Phi^n, \mathbf{U}^n$ and R_c^n, find $P^{n+1}, \{\mathbf{U}^{n+1}, \Phi^{n+1}\}$ by fixed-stress iteration method;
5:     Given C^n, Φ^n, P^{n+1} and R_c^n, find C^{n+1};
6: **until** $\max\{Res(P), Res(\Theta), Res(C), Res(\mathbf{U}, \Phi)\} \leq \text{TOL}_s$
7: Apply adaptive mesh refinement in Algorithm 1;
8: Increment $t^{n+1} \rightarrow t^{n+2}$.
___

a   b   c   d
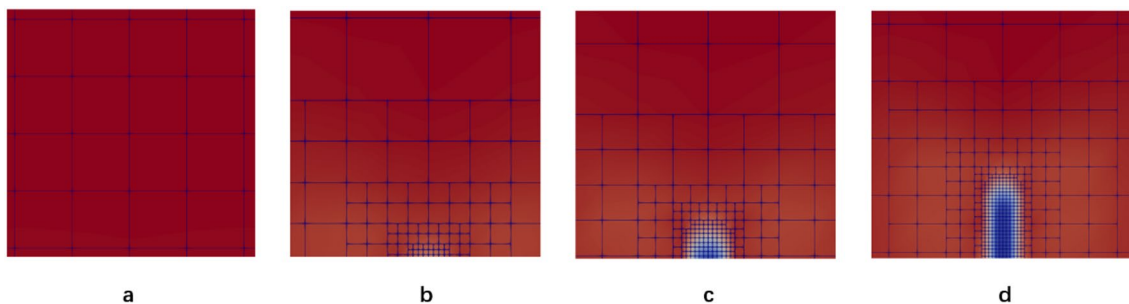
Fig. 2 Predictor–corrector adaptive mesh refinement: **a** the big mesh is used for initial refinement globally. **b** When there is a tendency to fracture at any point, return to the previous time step and refine the mesh in the possible fracture area, and re-solve the solution variables. **c** Recalculate the solution for this time step on the fine grid; **d** Repeat the above steps until the fracture path positions are all the minimum size mesh
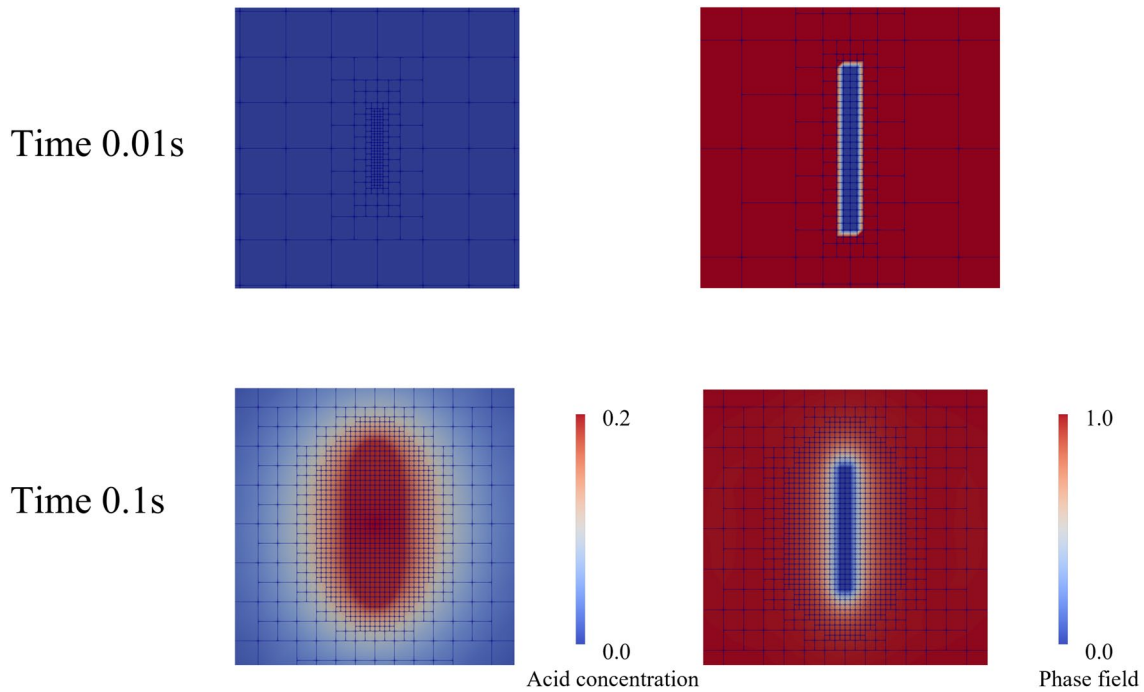
Fig. 3 Extended adaptive mesh refinement in Case #1. In time 0.01s, the acid fluid was injected a little and the mesh was refined around the initial fracture. In time 0.1s, the acid fluid fills the fracture and leaks into the reservoir. The mesh would be refined based on the acid region at that time

**Fig. 4** Solving schemes for coupled system in timestep t^{n+1}
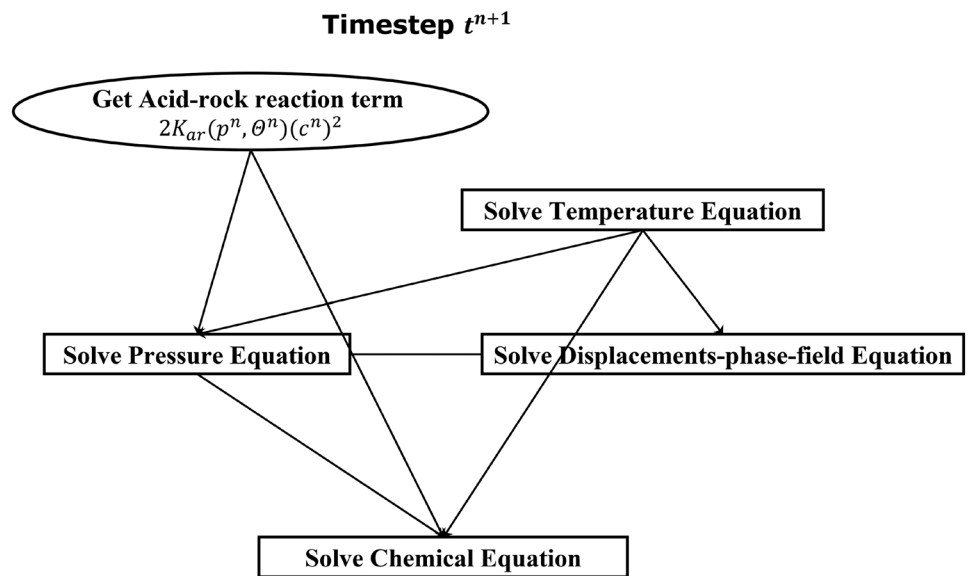
4 Numerical Experiments

In this section, we conducted some numerical experiments to demonstrate the capabilities of our model. All experiments were computed with a version of IPACS (Wheeler et al. 2020), which uses modulus of the open-source pfm-cracks code

(Heister and Wick 2020) and the open-source finite element package deal.II (Arndt et al. 2017).

Domain and initial fracture For all numerical tests, the global domain was $\Lambda = (0, 4\,m)^2$ and the injection point was $(2\,m, 2\,m)$. The initial fracture was set at the center, which is shown in Fig. 5.

Material parameters The material parameters are shown in Table 1, which were used for all numerical tests.
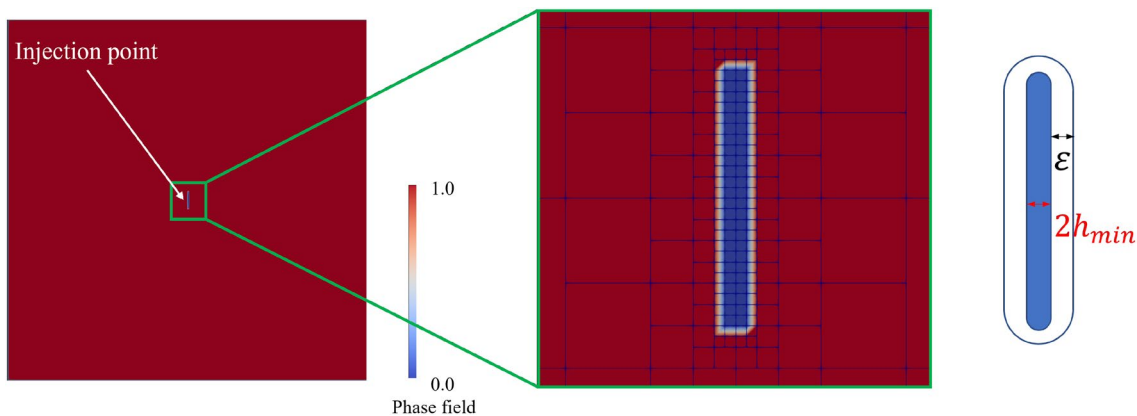
Fig. 5 Initial fracture setting in two-dimensional porous media. At that time, the acid fluid was not injected and the mesh was refined only based on the phase field

Source terms From a physical perspective, the heat and acid would be injected with fluid during acid fracturing. The source terms of the chemical equation were described in Sect. 4.2. The source terms of the pressure equations were defined by Peaceman's model: (Lee et al. 2016c; Peaceman 1978, 1983):

$$q_{Ff} = c_{Fp}(p_b - p) \times H_p(x),$$

$$q_{Rf} = c_{Rp}(p_b - p) \times H_p(x),$$

$$H_p(x) = \begin{cases} 1 & \text{if } \|x - X\| < r \\ 0 & \text{otherwise} \end{cases}. \tag{59}$$

The source terms of the temperature equations were defined as:

$$q_{F\Theta} = c_{F\Theta}q_{Ff}, \quad q_{R\Theta} = c_{R\Theta}q_{Rf}. \tag{60}$$

Here, p_b was the given wellbore pressure. $c_{Fp} > 0$ and $c_{Rp} > 0$ were the pressure injection constants. $c_{F\Theta} \in \mathbb{R}$ and $c_{R\Theta} \in \mathbb{R}$ were the temperature injection constants. r was small positive constant, X was the injection point in the domain.

Test cases Based on the given material parameters, we propose the following numerical tests to study the acid fracture behavior:

- Case #1: Acid fracture propagation in an elastic medium with single acid injection;
- Case #2: Artificial fracture propagation without acid effects;
- Case #3: Artificial fracture propagation without thermal and acid effects;
- Case #4: Acid fracture propagation with autogenic acid injection;
- Case #5: Acid fracture propagation affected by the natural hole. The coordinate of the hole center is $(2.1m, 2.5m)$ and the radius is $0.01m$;

Table 1 Table to material parameters

Symbol	Material parameter	Quantity	Unit
G_F	Critical energy release rate	1.0×10^{10}	N/m
E_0	Initial Young's modulus	10	GPa
v_0	Initial Poisson ratio	0.2	–
η_F	Fracture viscosity	1.0	$mPa \cdot s$
η_R	Reservoir viscosity	1.0	$mPa \cdot s$
K_{Fd}	Fracture thermal diffusion coefficients	2.0	$W/(m \cdot K)$
K_{Rd}	Reservoir thermal diffusion coefficients	0.2	$W/(m \cdot K)$
C_F	Fracture heat capacity coefficients	4.2	$kJ/(kg \cdot K)$
C_R	Reservoir heat capacity coefficients	1.0	$kJ/(kg \cdot K)$
φ_R^0	initial porosity of reservoir	0.1	–
α	Biot coefficient	1.0	–
M	Biot modulus	1.0×10^8	Pa
K_{tc}	Thermal expansion coefficient of pores	5.0×10^{-6}	$1/K$
ρ_{Ff}^0	Initial fluid densities in fracture	1000.0	kg/m^3
ρ_{Rf}^0	Initial fluid densities in reservoir	1000.0	kg/m^3
ρ_{Rr}	Rock densities in reservoir	2500.0	kg/m^3

- Case #6: Acid fracture propagation affected by the natural hole. The coordinate of the hole center is $(2.15m, 2.5m)$ and the radius is $0.01m$;
- Case #7: Acid fracture propagation affected by the natural hole. The coordinate of the hole center is $(2.25m, 2.5m)$ and the radius is $0.01m$;
- Case #8: Acid fracture propagation affected by the natural hole. The coordinate of the hole center is $(2.5m, 2.5m)$ and the radius is $0.01m$;

- Case #9: Acid fracture propagation affected by the natural hole. The coordinate of the hole center is $(2.25m, 2.5m)$ and the radius is $0.02m$;
- Case #10: Acid fracture propagation affected by the natural hole. The coordinate of the hole center is $(2.25m, 2.5m)$ and the radius is $0.04m$;
- Case #11: Acid fracture propagation affected by natural fracture. The angle of the natural fracture is 90°;
- Case #12: Acid fracture propagation affected by natural fracture. The angle of the natural fracture is 45°;
- Case #13: Acid fracture propagation affected by natural fracture. The angle of the natural fracture is 20°;
- Case #14: Acid fracture propagation in complex reservoirs.

Quantities of interest (QoI) In our numerical tests, we compared graphical solutions and studied the following quantities of interests:

1. Fracture volume (*FV*) (It is fracture area in 2D system)

$$F_V = \int_\Lambda \mathbf{u} \nabla \phi d\mathbf{x}. \tag{61}$$

2. Crack opening displacements (*COD*) on the line $y = y_c$

$$COD = \int_0^4 \mathbf{u}(x, y_c) \nabla \phi(x, y_c) d\mathbf{x}. \tag{62}$$

3. Acid consumption(*AC*)

$$A_c = 2 \int_\Lambda K_{ar}(p, \Theta) \varphi_R^* c^2(x) d\mathbf{x}. \tag{63}$$

4.1 Model Verification with Sneddon Fracture

In Case #1, Case #2 and Case #3, we considered the standard Sneddon setting (Sneddon and Lowengrub 1969; Bueckner 1971) in an elastic medium to verify the model, which is nowadays considered as a benchmark (Wheeler et al. 2014; Bourdin et al. 2012; Schröder et al. 2021; Chukwudozie et al. 2019). The fluid pressure, temperature and acid etching were studied during the fracture propagation. The simulation result of Case#1 is shown in Fig. 6.

The numerical tests were computed in a quasi-stationary manner. We chose different adaptive mesh refinements to study their impact on the QoIs in Case #1. The initial meshes were both five times uniformly refined, and local mesh adaptivity was applied for five further levels. The refined threshold for refinement scheme A was set as $\phi(x) < TH_\phi$. The refined thresholds for refinement scheme B were set as $\phi(x) < TH_\phi$ or $c(x) > TH_c$. The results are shown in Fig. 7.

As shown in Fig. 7, the calculation results of QoIs exhibit variations depending on the refinement scheme. Higher-level refined meshes would contribute to more accurate and smoother results. When the mesh was refined based on the phase-field variables in Scheme A, the calculation results of fracture volume and COD were close to those in Scheme B. However, there is a disparity in the results for the acid consumption between Scheme A and Scheme B. Here, Scheme B, which takes the acid solution into consideration, leads to a smoother result. This difference can be attributed to the fact that the acid consumption is closely related to acid etching, as described in Eq. (63). For improved simulation results in the acid fracture problem, it is necessary to refine the mesh based on both the fracture area and the acid-etched area.

Next, the extended adaptive mesh refinement (outlined in Sect. 3.6) was employed to verify computationally the convergence. The results are shown in Fig. 8. The global refinements were fixed at level 5 and local refinements were employed to study the change of fracture volume for different mesh sizes. The qualitative numerical stability of this model is thus demonstrated since the fracture volume curve variation becomes smaller on finer meshes.

Then, the extended adaptive mesh refinement (again Sect. 3.6) was also applied to the following Cases. The fracture volume and COD results of Case#1, Case#2 and Case #3 are shown in Fig. 9. It can be observed that both the acid and thermal effects lead to an increase in fracture volume and COD during acid fracture propagation. The initiation time of fracture in the same y_c would decrease with the effect of thermal stress and acid etching. The thermal stress would appear as tensile stress and play an auxiliary role in fracture propagation. The acid etching would decrease the strength of the rock and increase the fracture volume and COD. Similar findings about the acid and thermal effects have been carried out by Khoei et al. (2012); Fan et al. (2019).

4.2 Settings for Single Acid Injection and Autogenic Acid Injection

During acid fracturing, acid would be injected into the reservoirs in various methods (Du et al. 2022; Malagon et al. 2008; Aljawad et al. 2020). The single acid injection is a simple and low-cost method. The acid fluid would be injected into the reservoirs directly through the wellbore, which may result in limited fracture coverage and may damage the wellbore. The autogenic acid fluid system is another popular acid system (Wang et al. 2020; Lei et al. 2021). Unlike conventional acid fluids, which are prepared by mixing strong acids with water and other additives, the autogenic acid fluid system would produce the acid by chemical reactions in reservoirs. It would cause less damage to the wellbore and reduce the risk to workers. Different
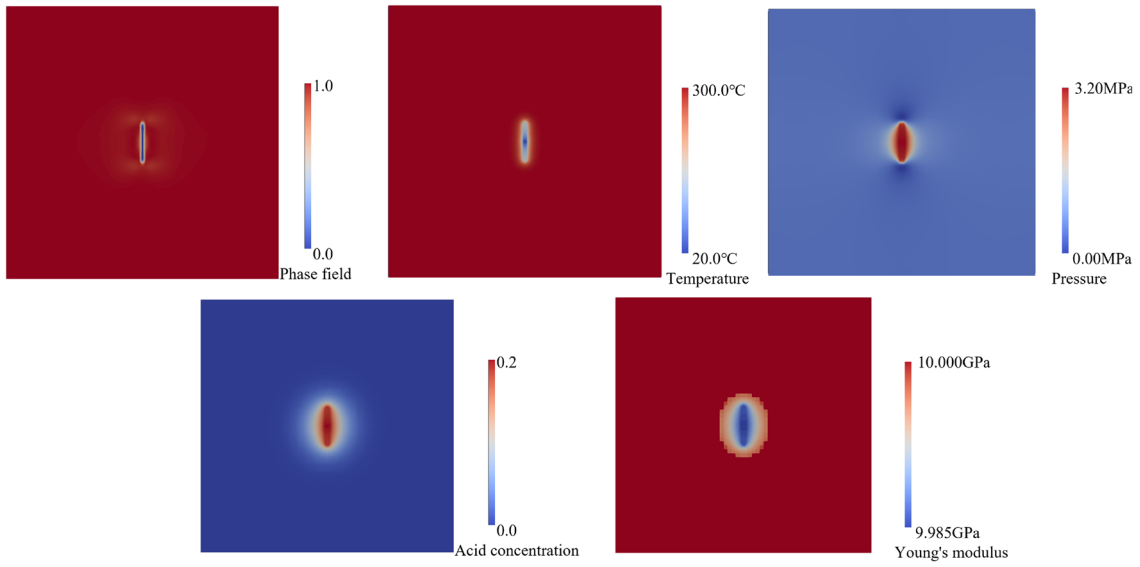
Fig. 6 Acid fracture propagation in Case #1 at time 0.15s. The acid fracture began in the homogeneous media and the Young's modulus decreased with the acid etching
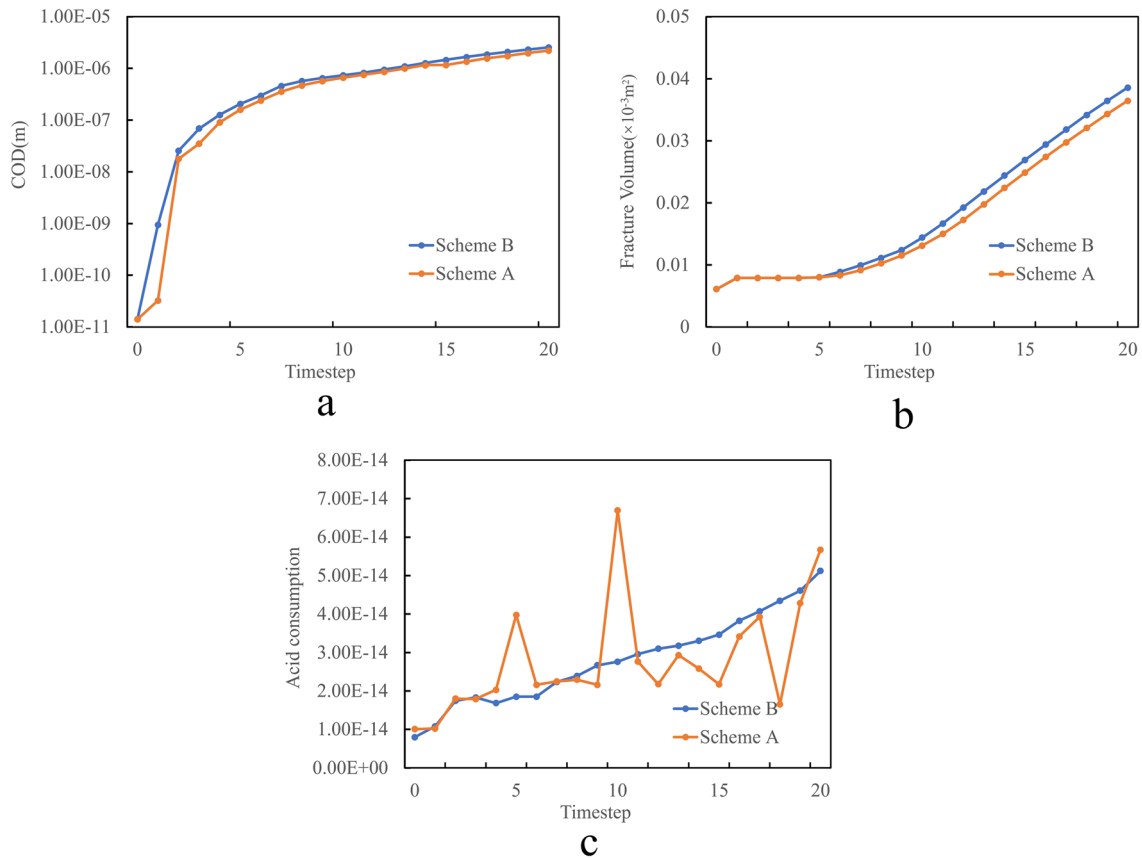
Fig. 7 The effect of different refinement schemes on QoIs: **a**, Fracture volume; **b**, Crack opening displacements($y_c = 2.5m$); **c**, Acid consumption. The timestep size was $0.01s$. The mesh was 5 times uniformly refined and 4 times locally
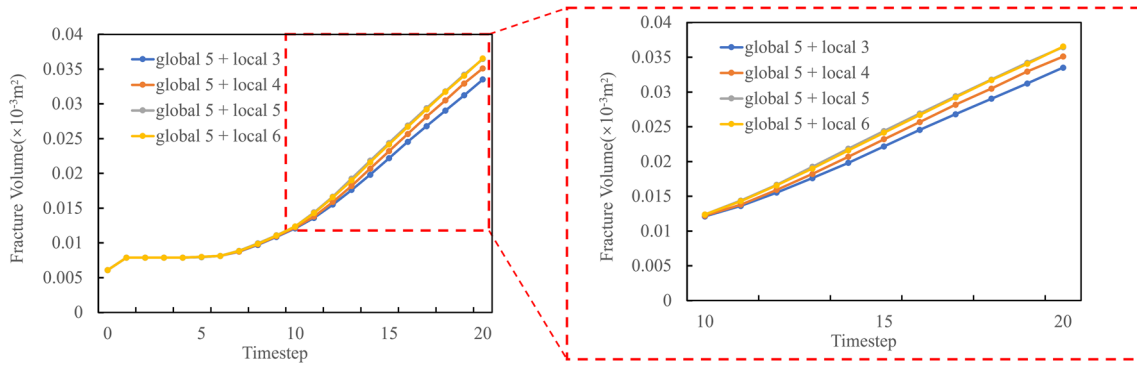
Fig. 8 Acid fracture propagation in Case #1 with different mesh size. The extended adaptive mesh refinement was used and the global refinements were fixed as 5 times. The fracture volume curve variation becomes smaller on finer meshes
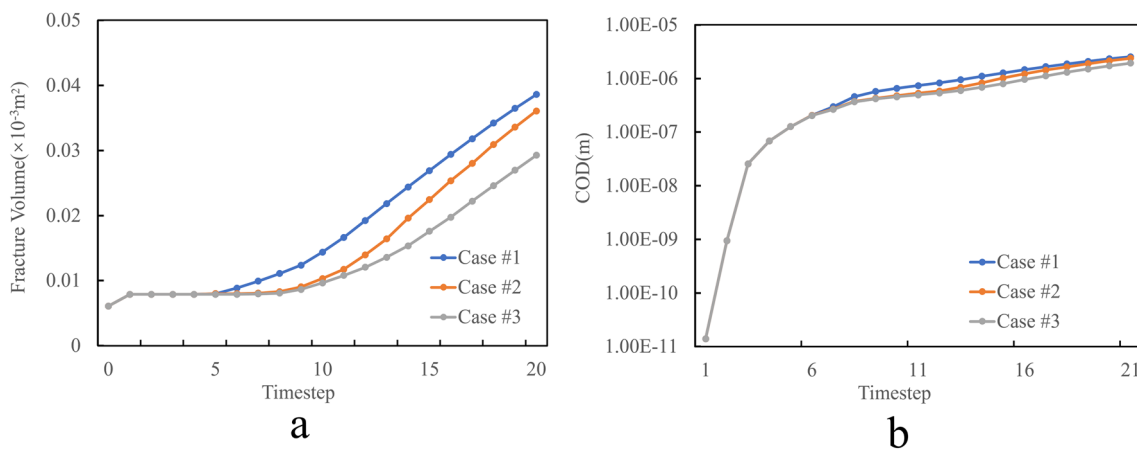
Fig. 9 The fracture volume and COD results of Case#1, Case#2 and Case #3.The timestep size was $0.01s$: a,Fracture volume; b,Crack opening displacements($y_c = 2.5m$)

injection methods require specific settings on the injection term in the chemical equation. Here, we proposed two settings for q_{Fc} and q_{Rc} to describe the single acid injection and autogenic acid injection. For single acid injection, we have:

$$
\begin{aligned}
q_{Fc} &= c_{Fc}c_{Fp}(p_b - p) \times H_c(x) , \\
q_{Rc} &= c_{Rc}c_{Fp}(p_b - p) \times H_c(x) , \\
H_c(x) &= \begin{cases} 1 & \text{if } \|x - X\| < r \\ 0 & \text{otherwise} \end{cases} .
\end{aligned}
\tag{64}
$$

Here, c_{Fc} and c_{Rc} were the chemical injection constants, r was a small positive constant, X was the injection point in the domain. Finally, p_b, c_{Fp} and c_{Rp} were defined in Eq. (59).

For the autogenic acid injection in Case #4, the source term was defined as:

$$
\begin{aligned}
q_{Fc} &= c_{Fc}C_{Fs}(p, \Theta) \times H_c(x) , \\
q_{Rc} &= c_{Rc}C_{Rs}(p, \Theta) \times H_c(x) , \\
H_c(x) &= \begin{cases} 1 & \text{if } p(x) > p_r \cap \Theta(x) > \Theta_r \\ 0 & \text{otherwise} \end{cases}
\end{aligned}
\tag{65}
$$

Here, $C_{Fs}(p, \Theta)$ and $C_{Fs}(p, \Theta)$ were the acid production functionals, and p_r and Θ_r were the threshold values for the autogenic acid production. The acid fracture shapes under different injection methods are shown in Fig. 10.

It was observed that different injection methods would lead to different etching results. The autogenic acid injection methods would etch the formation uniformly, which is good for further development. The simulation results show agreement with practical field experiences (Liu et al. 2014; Hou et al. 2019).
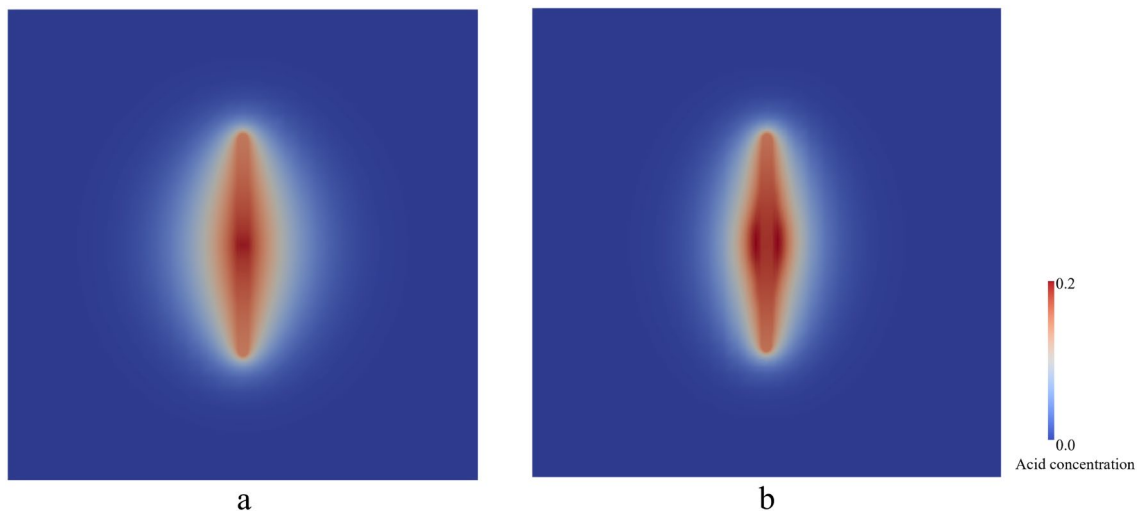
Fig. 10 Acid fracture propagation under different acid injection methods at time 0.4*s*: **a**. single acid injection **b**. autogenic acid injection. Compared with the single acid injection, the acid concentration under autogenic acid injection was more uniform

4.3 Effect of the Natural Holes on Acid Fracture Propagation

Natural structures would affect the propagation of artificial fractures (Dai et al. 2021; Gou et al. 2021). In this section, we simplified the natural holes into circles and studied the effect of natural holes on acid fracture propagation.

As we observed in Fig. 11, the effect of the single natural hole on acid fracture would change with the distance and hole size. The acid fracture would turn its propagation direction to the hole. If the distance was sufficiently close and the hole size was big enough, acid fracture would penetrate the natural hole. If the distance was not close or the hole size was not big enough, the acid propagation path would only be close to the hole location. If the distance was far away, the natural holes would have no influence on acid fracture propagation. Similar studies about natural holes with analogous findings have been carried out by Bing et al. (2022); Jiawei et al. (2020).

4.4 Effect of the Natural Fractures on Acid Fracture Propagation

Natural fractures often exist in carbonate reservoirs, which may affect the propagation of artificial fractures (Gou et al. 2021). In Case #11, Case #12 and Case #13, we studied the interaction between acid fracture and natural fractures to validate our model. In this simulation, we simplified the natural fractures into straight slits.

As we observed in Fig. 12. The effect of the single natural fracture would be affected by the angle between acid fracture and natural fracture. When the acid fracture intersected the natural fracture, it would go into the natural fracture and re-initiate at the end of the natural fracture. The re-initiation direction would be determined by the angle of the natural fracture. Similar studies about natural fractures with analogous findings have been carried out by Li et al. (2018); Jiawei et al. (2020).

In addition to the single natural fracture and the hole, we also conducted numerical experiments with multiple fractures and holes, which are easy to find in complex carbonate reservoirs. The simulation result is shown in Fig. 13. The randomness of acid fracture propagation was stronger in complex formations. Due to the limitations of rock samples in physical experiments, it is necessary to develop numerical models to study acid fracture propagation in complex formations.

5 Guidance for the Validation Experiment Based on the Phase-Field Idea

Researchers have observed that natural fractures and holes affect artificial fracture propagation (Lee and Wheeler 2021), which has been proved by many physical experiments (Hou et al. 2021; Dai et al. 2021). From an engineering point of view, accuracy and correctness are paramount in numerical simulations within complex geological formations (Weng 2015; Ju et al. 2019). Unfortunately, analytical solutions of acid fracture in fracture-hole formation are hard to get. Based on the phase-field method, we can design new visual experimental equipment for 2D fracture propagation (Fig. 14) and propose a quantitative method for assessing the accuracy and correctness of numerical simulations.
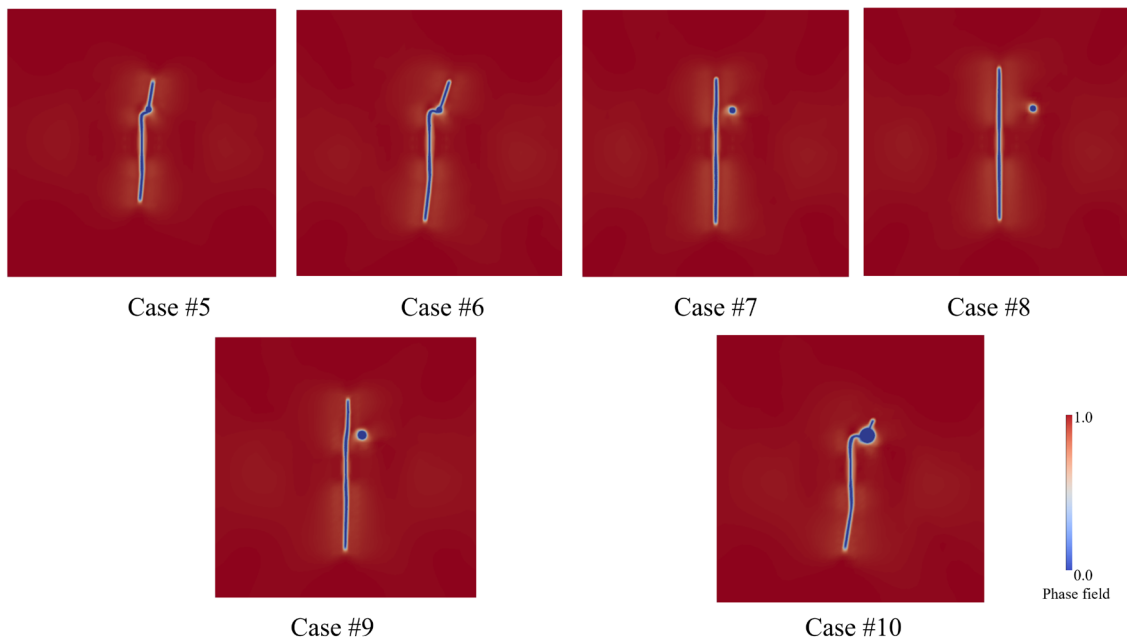
Fig. 11 Effect of the natural holes on the acid fracture propagation at time $0.4\,s$. The attraction effect of natural holes to acid fractures would decrease with the distance and increase with the size of natural holes. When the distance was 0.1 m (Case #5) and 0.15 m (Case #6), the acid fractures would penetrate the natural hole. When the distance was 0.25 m (Case #7), the acid fracture would turn its propagation direction. When the distance was 0.5m (Case #8), the natural hole had nearly no influence on the acid fracture propagation. When the distances were the same, the attraction effect of natural holes to acid fractures would increase with the size of the natural holes. The acid fracture would turn its propagation (Case #9) and penetrate the natural hole (Case #10) with the hole size increasing
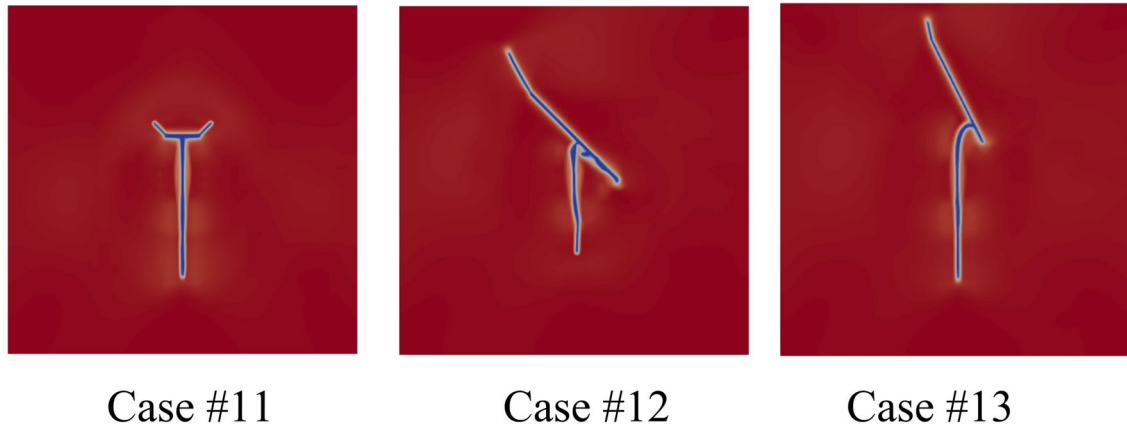

Fig. 12 Effect of the natural fractures on the acid fracture propagation at time $0.4s$. The acid fractures would grow into the natural fracture and re-crack at the end of the natural fracture. When the angle between the natural fracture and acid fracture was 90°, the fracture would re-crack at both sides uniformly. With the angle decreasing, the propagation speed and re-crack direction would be different at both sides

First, we would prepare a rock plate with natural fractures and holes, as shown in Fig. 14. The plate can be obtained from an outcrop or artificial rock source. Next, we would load the rock plate into the visual experimental equipment. By injecting fluid into the center of the plate, we can observe and record the propagation of fractures.

Afterward, we need to perform numerical simulations based on the characteristics of the rock plate. Since the numerical simulation and physical simulation have the same size and characteristics, we can define a difference function based on the concept of the phase-field method. The mesh from the numerical simulation can be extracted

Fig. 13 Acid fracture propagation in complex reservoirs. Fracture propagation was influenced by multiple factors and presented strong randomness

Time 0

Time 0.3s
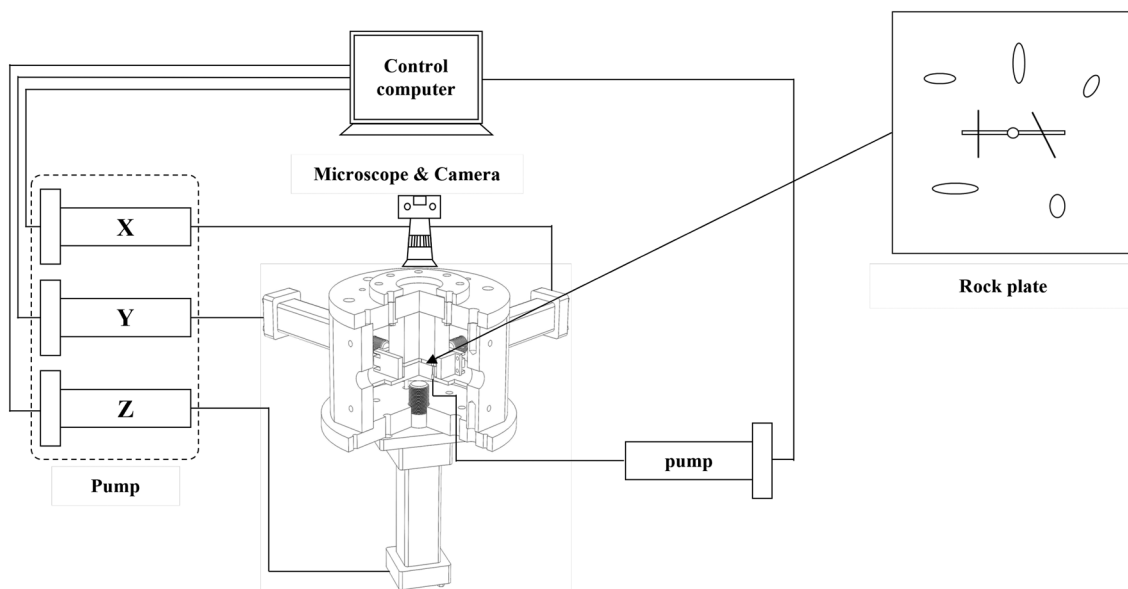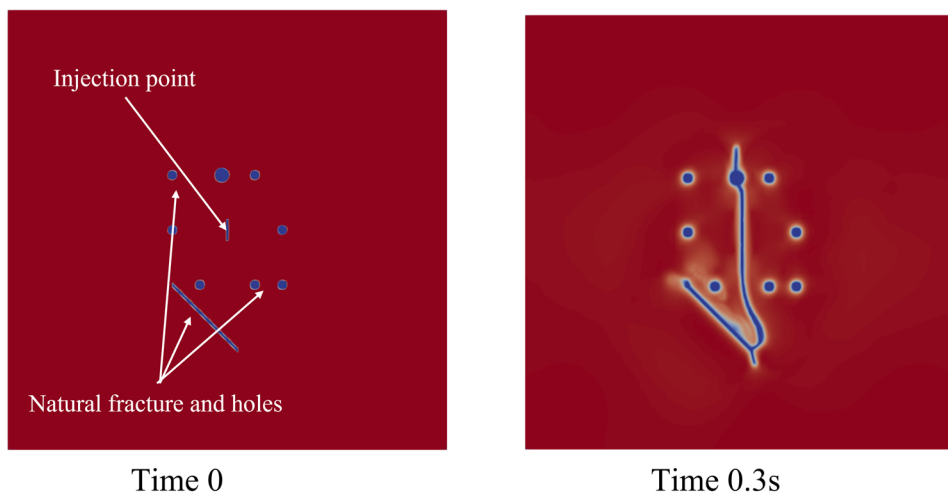
Fig. 14 Visual experimental equipment for fracture propagation in two-dimensional rock plate. The boundary conditions would be controlled by the computer and the pumps. The rock plate size is $100mm \times 100mm$

and mapped to the results of the physical simulation (Fig. 15).

We use $\phi_p = 0$ to represent the fracture and $\phi_p = 1$ to represent the non-fractured rock, and ϕ_n is the numerical simulation result at the corresponding node (n_m is the number of nodes). The local difference function and global difference function can be defined as:

$$D_{\text{local}} = |\phi_p - \phi_n| \quad \text{and} \quad D_{\text{global}} = \frac{1}{n_m} \sum_0^{n_m} D_{\text{local}}. \quad (66)$$

If the difference function is large, it indicates that there is a significant disparity between numerical simulations and physical simulations, resulting in lower accuracy of the numerical model. The difference function's outcome is evidently influenced by the resolution. There are some conflicts related to adaptive mesh refinement. Additionally, improvements are needed for the acid-proofing of the visual experimental equipment. Even though the accuracy evaluation method is in need of improvement, the comparison method using the difference function establishes a connection between physical experiments and numerical simulations. We believe it can assist petroleum engineers in quantitatively assessing numerical models.

Fig. 15 The phase-field value on rock plate from the physical experiment. Random natural holes in the rock will affect the propagation of the artificial fracture. By using image technology, the phase-field value on the rock plate can be gotten and used to evaluate the accuracy of numerical simulation quantitatively

6 Conclusion

In this paper, we modeled acid fracture employing a phase-field approach. Therein, we considered the influences of temperature, pressure, and acid etching, resulting into a THMC (Thermo-Hydro-Mechanical-Chemical) model. Numerically, we used a quasi-monolithic scheme to solve displacements and phase-field variables, while partitioned schemes were employed to solve temperature, pressure, and acid concentration. This coupling scheme performed effective in presented numerical simulations. We extended the adaptive mesh refinement technique to consider the acid etching effects in the fracture area. This enhancement provides high resolution in the area of interest while keeping computational costs reasonably low. In addition to these advancements in the solution algorithm, we conducted several numerical experiments for verifications and validations. We demonstrated the computational capabilities for the presented phase-field approach for studying acid fracture propagation, including different types of acid injection and complex geological reservoir domains. The computational stability of the proposed model was also investigated through these numerical experiments. The main concluding remarks are summarized as follows:

1. The acid fracture propagation is affected by several factors. The acid and thermal effect would increase the fracture volume and fracture width. The natural fracture and holes would affect the fracture propagation direction. The randomness of acid fracture propagation is strong in complex formations. This study shows once more that it remains necessary to develop numerical models continuously to compensate for the shortage of physical experiments.

2. The temperature equations and the coupling terms were implemented into the model. The acid equations including diffusion, transport and reaction are derived based on the penalization method. The overall algorithm is of iterative coupling type. The proposed model performs well in complex engineering conditions. The numerical stability of this model was demonstrated by several simulations.

3. Acid fracture is a dynamic heterogeneous problem. Independently, whether the fracture grows in homogeneous media or heterogeneous media, the rock parameter would change with the acid etching. Thus, the acid area and fracture area are both important regions that need small mesh sizes during numerical simulations. For the dynamic heterogeneous problem, the extended adaptive mesh refinement can be used to get higher accuracy and saving in the computational costs.

Data availability The authors confirm that the data supporting the findings of this study are available within the article and data will be made available on request.

Declarations

Conflict of interest The authors have no relevant financial or non-financial interests to disclose.

References

Adachi J, Siebrits E, Peirce A et al (2007) Computer simulation of hydraulic fractures. Int J Rock Mech Min Sci 44:739–757
Aldakheel F, Noii N, Wick T et al (2021) A global-local approach for hydraulic phase-field fracture in poroelastic media. Comput Math Appl 91:99–121
Aljawad MS, Schwalbert MP, Zhu D et al (2020) Improving acid fracture design in dolomite formations utilizing a fully integrated acid fracture model. J Petrol Sci Eng 184:106481
Ambati M, Gerasimov T, De Lorenzis L (2015) A review on phase-field models of brittle fracture and a new fast hybrid formulation. Comput Mech 55(2):383–405

Ambrosio L, Tortorelli V (1990) Approximation of functionals depending on jumps by elliptic functionals via γ-convergence. Comm Pure Appl Math 43:999–1036

Ambrosio L, Tortorelli V (1992) On the approximation of free discontinuity problems. Boll Un Mat Ital B 6:105–123

Arndt D, Bangerth W, Davydov D, et al (2017) The deal. ii library, version 8.5. J Numer Math 25(3) :137–145

Arrhenius S (1889) Über die dissociationswärme und den einfluss der temperatur auf den dissociationsgrad der elektrolyte. Zeitschrift für physikalische Chemie 4(1):96–116

Bai B, He Y, Li X et al (2017) Experimental and analytical study of the overall heat transfer coefficient of water flowing through a single fracture in a granite core. Appl Thermal Eng 116:79–90

Bing H, Dai Yifan FM, Kunpeng Z et al (2022) Numerical simulation of pores connection by acid fracturing based on phase field method. Acta Petrolei Sinica 43(6):849

Bourdin B, Francfort GA (2019) Past and present of variational fracture. SIAM News 52 (9)

Bourdin B, Francfort GA, Marigo JJ (2000) Numerical experiments in revisited brittle fracture. J Mech Phys Solids 48(4):797–826

Bourdin B, Francfort G, Marigo JJ (2008) The variational approach to fracture. J Elasticity 91(1–3):1–148

Bourdin B, Chukwudozie C, Yoshioka K (2012) A variational approach to the numerical simulation of hydraulic fracturing. SPE Journal, Conference Paper 159154-MS

Bueckner HF (1971) Crack problems in the classical theory of elasticity (in sneddon and m. lowengrub)

Castonguay S, Mear M, Dean R, et al (2013) Predictions of the growth of multiple interacting hydraulic fractures in three dimensions. SPE-166259-MS pp 1–12

Chong ZR, Yang M, Khoo BC et al (2016) Size effect of porous media on methane hydrate formation and dissociation in an excess gas environment. Ind Eng Chem Res 55(29):7981–7991

Chukwudozie C, Bourdin B, Yoshioka K (2019) A variational phase-field model for hydraulic fracturing in porous media. Comput Methods Appl Mech Eng 347:957–982

Coussy O (2004) Poromechanics. John Wiley & Sons

Dai Y, Hou B, Zhou C et al (2021) Interaction law between natural fractures-vugs and acid-etched fracture during steering acid fracturing in carbonate reservoirs. Geofluids 2021:1–16

Diehl P, Lipton R, Wick T et al (2022) A comparative review of peridynamics and phase-field models for engineering fracture mechanics. Comput Mech 69:1259–1293

Du J, Guo G, Liu P et al (2022) Experimental study on the autogenic acid fluid system of a high-temperature carbonate reservoir by acid fracturing. ACS Omega 7(14):12066–12075

Fan C, Luo M, Li S et al (2019) A thermo-hydro-mechanical-chemical coupling model and its application in acid fracturing enhanced coalbed methane recovery simulation. Energies 12(4):626

Fei F, Costa A, Dolbow JE, et al (2023) Phase-field simulation of near-wellbore nucleation and propagation of hydraulic fractures in enhanced geothermal systems (egs) . In: SPE Reservoir Simulation Conference, OnePetro

Francfort G, Marigo JJ (1998) Revisiting brittle fracture as an energy minimization problem. J Mech Phys Solids 46(8):1319–1342

Ghidelli M, Sebastiani M, Johanns KE et al (2017) Effects of indenter angle on micro-scale fracture toughness measurement by pillar splitting. J Am Ceramic Soc 100(12):5731–5738

Gou B, Zhan L, Guo J et al (2021) Effect of different types of stimulation fluids on fracture propagation behavior in naturally fractured carbonate rock through ct scan. J Petrol Sci Eng 201:108529

Guo J, Liu H, Zhu Y et al (2014) Effects of acid-rock reaction heat on fluid temperature profile in fracture during acid fracturing in carbonate reservoirs. J Petrol Sci Eng 122:31–37

Gupta P, Duarte C (2014) Simulation of non-planar three-dimensional hydraulic fracture propagation. Int J Numer Anal Meth Geomech 38:1397–1430

Gupta P, Duarte CA (2016) Coupled formulation and algorithms for the simulation of non-planar three-dimensional hydraulic fractures using the generalized finite element method. Int J Numer Anal Methods Geomech 40(10):1402–1437

Gupta S, Deusner C, Haeckel M et al (2017) Testing a thermo-chemo-hydro-geomechanical model for gas hydrate-bearing sediments using triaxial compression laboratory experiments. Geochem Geophys Geosyst 18(9):3419–3437

Heider Y (2021) A review on phase-field modeling of hydraulic fracturing. Eng Fracture Mech 253:107881

Heider Y, Markert B (2017) A phase-field modeling approach of hydraulic fracture in saturated porous media. Mech Res Commun 80:38–46

Heider Y, Reiche S, Siebert P et al (2018) Modeling of hydraulic fracturing using a porous-media phase-field approach with reference to experimental data. Eng Fracture Mech 202:116–134

Heister T, Wick T (2020) pfm-cracks: A parallel-adaptive framework for phase-field fracture propagation. Softw Impacts 6:100045

Heister T, Wheeler MF, Wick T (2015) A primal-dual active set method and predictor-corrector mesh adaptivity for computing fracture propagation using a phase-field approach. Comput Methods Appl Mech Eng 290:466–495

Hou B, Zhang R, Chen M et al (2019) Investigation on acid fracturing treatment in limestone formation based on true tri-axial experiment. Fuel 235:473–484

Hou B, Dai Y, Zhou C et al (2021) Mechanism study on steering acid fracture initiation and propagation under different engineering geological conditions. Geomech Geophys Geo-Energy Geo-Resources 7(3):73

Jiang C, Hong C, Wang T et al (2023) N-side cell-based smoothed finite element method for incompressible flow with heat transfer problems. Eng Anal Boundary Elements 146:749–766

Jiawei K, Yan J, Kunpeng Z et al (2020) Experimental investigation on the characteristics of acid-etched fractures in acid fracturing by an improved true tri-axial equipment. J Petrol Sci Eng 184:106471

Ju M, Li J, Yao Q et al (2019) Rate effect on crack propagation measurement results with crack propagation gauge, digital image correlation, and visual methods. Eng Fracture Mech 219:106537

Khoei A, Moallemi S, Haghighat E (2012) Thermo-hydro-mechanical modeling of impermeable discontinuity in saturated porous media with x-fem technique. Eng Fracture Mech 96:701–723

Kuhn C, Müller R (2010) A continuum phase field model for fracture. Eng Fracture Mech 77(18):3625–3634

Lee S, Wheeler MF (2021) Modeling interactions of natural and two-phase fluid-filled fracture propagation in porous media. Comput Geosci 25:731–755

Lee S, Mikelić A, Wheeler MF et al (2016) Phase-field modeling of proppant-filled fractures in a poroelastic medium. Comput Methods Appl Mech Eng 312:509–541

Lee S, Reber JE, Hayman NW et al (2016) Investigation of wing crack formation with a combined phase-field and experimental approach. Geophys Res Lett 43(15):7946–7952

Lee S, Wheeler MF, Wick T (2016) Pressure and fluid-driven fracture propagation in porous media using an adaptive finite element phase field model. Comput Methods Appl Mech Eng 305:111–132

Lee S, Wheeler MF, Wick T (2017) Iterative coupling of flow, geomechanics and adaptive phase-field fracture including level-set crack width approaches. J Comput Appl Math 314:40–60

Lee S, Wheeler MF, Wick T et al (2017) Initialization of phase-field fracture propagation in porous media using probability maps of fracture networks. Mech Res Commun 80:16–23

Lee S, Mikelić A, Wheeler M et al (2018) Phase-field modeling of two phase fluid filled fractures in a poroelastic medium. Multiscale Modeling Simul 16(4):1542–1580

Lee S, Min B, Wheeler MF (2018) Optimal design of hydraulic fracturing in porous media using the phase field fracture model coupled with genetic algorithm. Comput Geosci 22:833–849

Lei J, Jia J, Liu B et al (2021) Research and performance evaluation of an autogenic acidic fracturing fluid system for high-temperature carbonate reservoirs. Chem Technol Fuels Oils 57:854–864

Li S, Ma H, Zhang H et al (2018) Study on the acid fracturing technology for high-inclination wells and horizontal wells of the sinian system gas reservoir in the sichuan basin. J Southwest Petroleum Univ (Sci Technol Ed) 40(3):146

Liu Z, Chen M, Zhang G (2014) Analysis of the influence of a natural fracture network on hydraulic fracture propagation in carbonate formations. Rock Mech Rock Eng 47(2):575–587

Luo Z, Zhang N, Zhao L et al (2020) An extended finite element method for the prediction of acid-etched fracture propagation behavior in fractured-vuggy carbonate reservoirs. J Petrol Sci Eng 191:107170

Malagon C, Pournik M, Hill AD (2008) The texture of acidized fracture surfaces: implications for acid fracture conductivity. SPE Prod Oper 23(03):343–352

Melendez MG, Pournik M, Zhu D, et al (2007) The effects of acid contact time and the resulting weakening of the rock surfaces on acid-fracture conductivity. In: European Formation Damage Conference, OnePetro

Miehe C, Mauthe S (2016) Phase field modeling of fracture in multi-physics problems. part iii. crack driving forces in hydro-poro-elasticity and hydraulic fracturing of fluid-saturated porous media. Comput Methods Appl Mech Eng 304:619–655

Miehe C, Welschinger F, Hofacker M (2010) Thermodynamically consistent phase-field models of fracture: variational principles and multi-field fe implementations. Int J Numer Methods Eng 83(10):1273–1311

Miehe C, Hofacker M, Schaenzel LM et al (2015) Phase field modeling of fracture in multi-physics problems. part ii. coupled brittle-to-ductile failure criteria and crack propagation in thermo-elastic-plastic solids. Comput Methods Appl Mech Eng 294:486–522

Miehe C, Mauthe S, Teichtmeister S (2015) Minimization principles for the coupled problem of darcy-biot-type fluid transport in porous media linked to phase field modeling of fracture. J Mech Phys Solids 82:186–217

Miehe C, Schaenzel LM, Ulmer H (2015) Phase field modeling of fracture in multi-physics problems. part i. balance of crack surface and failure criteria for brittle crack propagation in thermo-elastic solids. Comput Methods Appli Mech Eng 294:449–485

Mikelić A, Wheeler MF (2012) Convergence of iterative coupling for coupled flow and geomechanics. Comput Geosci 17(3):455–462

Mikelić A, Wheeler M, Wick T (2013) A phase-field approach to the fluid filled fracture surrounded by a poroelastic medium, iCES Report 13-15

Mikelić A, Wheeler MF, Wick T (2015) A phase-field method for propagating fluid-filled fractures coupled to a surrounding porous medium. SIAM Multiscale Model Simul 13(1):367–398

Mikelić A, Wheeler MF, Wick T (2015) A quasi-static phase-field approach to pressurized fractures. Nonlinearity 28(5):1371

Min L, Wang Z, Hu X et al (2023) A chemo-thermo-mechanical coupled phase field framework for failure in thermal barrier coatings. Comput Methods Appl Mech Eng 411:116044

Nguyen CL, Heider Y, Markert B (2023) A non-isothermal phase-field hydraulic fracture modeling in saturated porous media with convection-dominated heat transport. Acta Geotechnica

Noii N, Wick T (2019) A phase-field description for pressurized and non-isothermal propagating fractures. Comput Methods Appl Mech Eng 351:860–890

Ogata S, Yasuhara H, Kinoshita N et al (2018) Modeling of coupled thermal-hydraulic-mechanical-chemical processes for predicting the evolution in permeability and reactive transport behavior within single rock fractures. Int J Rock Mech Min Sci 107:271–281

Peaceman DW (1978) Interpretation of well-block pressures in numerical reservoir simulation (includes associated paper 6988). Soc Petrol Eng J 18(03):183–194

Peaceman DW (1983) Interpretation of well-block pressures in numerical reservoir simulation with nonsquare grid blocks and anisotropic permeability. Soc Petrol Eng J 23(03):531–543

Peirce A, Detournay E (2008) An implicit level set method for modeling hydraulically driven fractures. Comput Meth Appl Mech Eng 197:2858–2885

Pham TV, Trang HT, Nguyen HMT (2022) Temperature and pressure-dependent rate constants for the reaction of the propargyl radical with molecular oxygen. ACS Omega 7(37):33470–33481

Poulet T, Karrech A, Regenauer-Lieb K et al (2012) Thermal-hydraulic-mechanical-chemical coupling with damage mechanics using escriptrt and abaqus. Tectonophysics 526:124–132

Pournik M (2008) Laboratory-scale fracture conductivity created by acid etching. Texas A &M University

Rabczuk T, Bordas S, Zi G (2010) On three-dimensional modelling of crack growth using partition of unity methods. Comput Struct 88(23–24):1391–1411

Santillan D, Juanes R, Cueto-Felgueroso L (2017) Phase field model of fluid-driven fracture in elastic media: Immersed-fracture formulation and validation with analytical solutions. J Geophys Res 122 (4) :2565–2589. 2016JB013572

Schrefler BA, Secchi S (2012) A method for 3-d hydraulic fracturing simulation. Int J Fract 178:245–258

Schröder J, Wick T, Reese S et al (2021) A selection of benchmark problems in solid mechanics and applied mathematics. Arch Computat Methods Eng 28:713–751

Shiozawa S, Lee S, Wheeler MF (2019) The effect of stress boundary conditions on fluid-driven fracture propagation in porous media using a phase-field modeling approach. Int J Numer Anal Methods Geomech 43(6):1316–1340

Shu B, Zhu R, Elsworth D et al (2020) Effect of temperature and confining pressure on the evolution of hydraulic and heat transfer properties of geothermal fracture in granite. Appl Energy 272:115290

Sneddon IN, Lowengrub M (1969) Crack problems in the classical theory of elasticity. SIAM series in Applied Mathematics, John Wiley and Sons, Philadelphia

Suh HS, Sun W (2021) Asynchronous phase field fracture model for porous media with thermally non-equilibrated constituents. Comput Methods Appl Mech Eng 387:114182

Takabi B, Tai BL (2019) Finite element modeling of orthogonal machining of brittle materials using an embedded cohesive element mesh. J Manuf Mater Process 3(2):36

Tran D, Settari AT, Nghiem L (2013) Predicting growth and decay of hydraulic-fracture witdh in porous media subjected to isothermal and nonisothermal flow. SPE-J pp 781–794

Wang X, Li P, Qi T et al (2023) A framework to model the hydraulic fracturing with thermo-hydro-mechanical coupling based on the variational phase-field approach. Comput Methods Appl Mech Eng 417:116406

Wang Y, Zhou C, Yi X et al (2020) Research and evaluation of a new autogenic acid system suitable for acid fracturing of a high-temperature reservoir. ACS Omega 5(33):20734–20738

Weng X (2015) Modeling of complex hydraulic fractures in naturally fractured formation. J Unconventional Oil Gas Resources 9:114–135

Wheeler MF, Wick T, Wollner W (2014) An augmented-Lagrangian method for the phase-field approach for pressurized fractures. Comput Methods Appl Mech Eng 271:69–85

Wheeler MF, Wick T, Lee S (2020) IPACS: Integrated Phase-Field Advanced Crack Propagation Simulator. An adaptive, parallel, physics-based-discretization phase-field framework for fracture propagation in porous media. Comput Methods Appl Mech Eng 367:113124

Wick T (2020) Multiphysics Phase-Field Fracture: Modeling, Adaptive Discretizations, and Solvers. De Gruyter, Berlin, Boston

Wick T, Singh G, Wheeler M (2016) Fluid-filled fracture propagation using a phase-field approach and coupling to a reservoir simulator. SPE J 21(03):981–999

Wilson ZA, Landis CM (2016) Phase-field modeling of hydraulic fracture. J Mech Phys Solids 96:264–290

Wu JY, Nguyen VP, Nguyen CT et al (2020) Phase-field modeling of fracture. Adv Appl Mech 53:1–183

Wu L, Hou Z, Xie Y et al (2023) Fracture initiation and propagation of supercritical carbon dioxide fracturing in calcite-rich shale: a coupled thermal-hydraulic-mechanical-chemical simulation. Int J Rock Mech Min Sci 167:105389

Xu H, Cheng J, Zhao Z et al (2021) Coupled thermo-hydro-mechanical-chemical modeling on acid fracturing in carbonatite geothermal reservoirs containing a heterogeneous fracture. Renew Energy 172:145–157

Xue Y, Liu S, Chai J et al (2023) Effect of water-cooling shock on fracture initiation and morphology of high-temperature granite: application of hydraulic fracturing to enhanced geothermal systems. Appl Energy 337:120858

Yoshioka K, Bourdin B (2016) A variational hydraulic fracturing model coupled to a reservoir simulator. Int J Rock Mech Min Sci 88:137–150

Yu H, Taleghani AD, Lian Z (2019) On how pumping hesitations may improve complexity of hydraulic fractures, a simulation study. Fuel 249:294–308

Zhou B, Jin Y, Xiong W et al (2021) Investigation on surface strength of acid fracture from scratch test. J Petrol Sci Eng 206:109017

Zhou S, Zhuang X, Rabczuk T (2018) A phase-field modeling approach of fracture propagation in poroelastic media. Eng Geol 240:189–203

Zhou S, Zhuang X, Rabczuk T (2019) Phase-field modeling of fluid-driven dynamic cracking in porous media. Comput Methods Appl Mech Eng 350:169–198